Università
degli Studi
della Campania
Luigi Vanvitelli

Dipartimento di Matematica e Fisica

Investigation on an innovative pyro-electrohydrodynamic jet dispensing for accumulating low abundant biomolecules

DOCTOR OF PHILOSOPHY THESIS

CANDIDATE: Simona Itri

SUPERVISOR: Dr. Simonetta Grilli

2022

Table of Contents

List of publications

1. **Itri, S**., del Giudice, D., Mugnano, M., Tkachenko, V., Uusitalo, S., Kokkonen, A., ... & Grilli, S. **A Pin-Based Pyro-Electrohydrodynamic Jet Sensor for Tuning the Accumulation of Biomolecules Down to Sub-Picogram Level Detection.** Submitted and *Available at SSRN 4142162*.

2. **Itri, S.,** Gallo, M., Orefice, C., Garella, I., Di Domenico, M., Vitali, S., Stanzione, V., Grilli, S., Ferraro, P. and Nigro, R., 2022. **Oil Bodies Cream from Olive Paste: Extraction of a Functional Ingredient for Developing a Stable Food Emulsion**. *Applied Sciences*, *12*(12), p.6019.

3. Běhal, J., Valentino, M., Miccio, L., Bianco, V., **Itri, S**., Mossotti, R., Dalla Fontana, G., Stella, E. and Ferraro, P., 2022. **Toward an All-Optical Fingerprint of Synthetic and Natural Microplastic Fibers by Polarization-Sensitive Holographic Microscopy**. *ACS Photonics*, *9*(2), pp.694-705.

4. Valentino, M., Běhal, J., Bianco, V., **Itri, S.**, Mossotti, R., Dalla Fontana, G., Battistini, T., Stella, E., Miccio, L. and Ferraro, P., 2022. **Intelligent polarization-sensitive holographic flow-cytometer: Towards specificity in classifying natural and microplastic fibers.** *Science of The Total Environment*, *815*, p.152708.

5. Tkachenko, V., Schwödiauer, R., Rega, R., **Itri, S.**, Mugnano, M., del Giudice, D., Ottevaere, H., Nie, Y., Ferraro, P. and Grilli, S., 2022. **High-Rate Accumulation of Tiny Aqueous Droplets Using a Pyroelectrohydrodynamic Jet System.** *Advanced Engineering Materials*, *24*(3), p.2100756.

List of conference proceedings

1. D. del Giudice et al., **"Innovative biosensor for testing the astronaut health during spaceflight",** 2022 IEEE 9th International Workshop on Metrology for AeroSpace (MetroAeroSpace),2022, pp. 618-621.

2. Bianco, V., Valentino, M., Běhal, J., Pirone, D., **Itri, S**., Mossotti, R., Dalla Fontana, G., Stella, E., Miccio, L., Memmolo, P. and Ferraro, P., 2022, May. **Digital holography in microplastic identification.** In *Unconventional Optical Imaging III* (Vol. 12136, pp. 232-240). SPIE.

3. Cacace, T., **Itri, S.,** Rani, M., Federici, S., Miccio, L., Bianco, V., Paturzo, M. and Ferraro, P., 2021, October. **Compact holographic microscope for imaging flowing microplastics.** In *2021 International Workshop on Metrology for the Sea; Learning to Measure Sea Health Parameters (MetroSea)* (pp. 229-233). IEEE.

4. Rega, R., Mugnano, M., Del Giudice, D., **Itri, S.**, Tkachenko, V., Vespini, V., Coppola, S., Ferraro, P., Ottevaere, H., Nie, Y. and Uusitalo, S., 2021, June. **SensApp: a FET-open project for developing a supersensor able to detect Alzheimer's disease biomarkers in blood.** In *Optical Methods for Inspection, Characterization, and Imaging of Biomaterials V* (Vol. 11786, p. 1178605). SPIE.

5. Rega, R., Mugnano, M., Del Giudice, D., **Itri, S.**, Tkachenko, V., Vespini, V., Coppola, S., Mazzon, E., Oleandro, E., Ferraro, P. and Grilli, S., 2020, April. **Highly sensitive detection of low abundant molecules by pyro-electrohydro-dynamic jetting.** In *Biophotonics in Point-of-Care* (Vol. 11361, pp. 41-51). SPIE.

Introduction and aim of the work

The Ph.D. thesis presented here was developed in the framework of the European FET-Open Project called “SensApp”. SensApp stands for “Super-sensitive detection of Alzheimer’s disease biomarkers in plasma by an innovative droplet split-and stack approach”. The main goal of the project was the development of a new biosensing device based on an innovative technology, called “droplet split and stack” (DSS), able to dispense and accumulate very tiny droplets of body fluid samples and to detect biomarkers of the Alzheimer’s disease, such as β–amyloid and Tau proteins, with high sensitivity ($\leq$ 30 pg/mL). In fact, the search for these biomarkers in peripheral body fluids would help clinicians to perform non-invasive diagnosis avoiding the withdrawal of cerebrospinal fluid (CSF) from the patient. The project was carried out by a consortium of six partners consisting of three research organizations, two universities and one company. Specifically, the partners involved are the National Research Council of Italy with the Institute of Applied Sciences and Intelligent Systems (CNR-ISASI), in cooperation with the Department of Chemical, Materials and Production Engineering University of Naples ‘Federico II’, the Vrije Universiteit Brussel (VUB), Johannes Kepler University Linz (JKU), Technical Research Centre of Finland (VTT), “Bonino Pulejo” Clinical Centre, Ginolis Ltd Finland.

As far as biosensors are concerned, they are used in many fields such as screening of very small molecules as well as in pathologies that require a rapid detection of biomarkers and continuous monitoring. Biosensors can be divided into different categories according to their principles of operation such as enzyme-based, optical, and aptamer-based, just to name a few. Although their performance is sufficient for a wide range of applications, existing biosensors are struggling, when the biomarker concentration in biological samples is very low. In such cases, the limit of detection (LOD) of the standardized techniques often prevents the clinicians and/or the biologists from using the well-established biosensors to perform their studies. For example, one of the open issues is the current lack of a reliable technique for quantifying the levels of AD biomarkers in the peripheral blood of clinical patients. Nowadays this analysis can only be performed from CSF samples, which entail sufficient biomarker dosage. CSF sampling dramatically impacts the patient in terms of invasiveness and the health service in terms of hospitalization required for performing such tests. Moreover, the invasiveness of the procedure prevents clinicians to perform screening tests among the populations and follow-up therapies on full-blown patients. The gold standard for quantifying the levels of AD biomarkers in CSF is represented by ELISA-based procedures, which reach a LOD of around 50 pg/mL. Conversely, the level in the peripheral blood is expected to be much less than that value. It has been shown that an innovative label-free electrochemical protein sensor by Mun'delanji Vestergaard et al and a new colorimetric sensor by Ajay Piriya V.S. et al could reach the LOD above 10 pg/mL. This is an improvement to the current level of ELISA tests, but there is still a

need for improvement in sensitivity to reach the required level for peripheral blood. Different innovative techniques have been proposed in the literature to overcome the limit. These include mass spectrometry, immunoprecipitation and SIMOA. These methods have a high precision to identify and quantify the biomarker concentrations, but they include laborious and crucial pre-treatments of the sample that may reduce the level of reproducibility. Moreover, the complexity and costs of these procedures prevent their use in routine clinical assays.

In this scenario, I focused my PhD work on the implementation and characterization of the liquid dispensing technique that was then employed in the project for the development of the DSS technology mentioned previously. This technique makes use of the pyroelectric effect in a ferroelectric crystal such as the lithium niobate, and therefore we call it “pyro-electrohydrodynamic jet” (p-jet). Hereon, the device based on the p-jet technique will be called “p-jet sensor”, just for brevity. A reliable and reproducible configuration has been implemented and tested here for achieving high droplet repeatability and, simultaneously, for testing temperature variations non detrimental for the protein samples used as test model. Basically the sample is loaded in a commercial microarray-printing pin, which allowed to produce a stable meniscus profile from which the tiny droplets are ejected with high reproducibility. We used specific fluorescent probes to demonstrate the spots' reproducibility and successfully attain a linear trend of the fluorescent signal as a function of the number of accumulated jets, down to the sub-picogram level. Moreover, a comparative study is also accomplished by using a commercial piezo-driven bio-spotter. The results show the significantly higher performance of the p-jet in terms of molecule accumulation and subsequent fluorescence detection. The p-jet sensor was tested preliminarily for the case of the biomarker Aβ1-42 with concentrations in the picogram range. The results demonstrate for the first time the possibility to use the p-jet accumulation for immune-detection assays, with the key advantage to use a volume of the reaction below the microliter range.

Another important aspect studied in this work was the conformational stability and the chemical integrity of biomarkers involved in the disease diagnosis techniques. Some modifications of the protein conformation can lead to the formation of aggregates and, consequently, compromise the antibody’s capability to chemically bind the protein used in the immunoreaction assays, which are a gold standard in the clinical diagnosis of AD. The irreversible aggregations of these biomarkers could limit the antibody-antigen interaction, reducing the sensitivity and the specificity of the assay with a loss in terms of the intensity of the fluorescence signal. Therefore, a synthetic biomarker the Aβ1-42 solution was used as a model of the endogenous molecules to investigate the evolution of the protein folding and its consequence on fluorescent signal, and, on the ability to react with antibodies.

In this framework I focused my PhD work also on the determination of an easy method to verify the protein agglomeration which might influence the interaction with antibodies, thus the

sensitivity of the immunoreaction assay. Besides, protein aggregation has a crucial role in several neuropathological conditions and the understanding of this phenomenon may predict the progress of AD. It is not deeply comprehending the protein aggregation mechanism, the possible critical step in protein aggregation is the unfolding of the proteins. Unfolded proteins are more subject to aggregation. This change of configuration characterizes the aggregation and put the protein at risk to become a cause of disease such as AD. It is well known the importance of the analytical method for studying the protein agglomeration for defining pathophysiological events and finally for developing new therapies and better diagnostic tools. Several methods for investigating protein agglomeration exist, they range from the separation technique to dynamic light scattering and immunoassays. However, these analytical methods have some drawbacks, one of them is that it can be possible to induce or destroy aggregates during sample preparation or the loss of aggregates by adsorption onto the column during for example the size-exclusion chromatography. Moreover, no single analytical method can cover the entire size range in which aggregates may appear. Here, a non-destructive and simple method to investigate protein agglomeration is presented. This innovative method was characterized by surface tension measurements of Aβ1-42 solutions with a pendant drop tensiometer, then by the application of mathematical models for extrapolating kinetic parameters to evaluate the protein structure modifications. In the end, to verify the hypothesis about the influence of the protein agglomeration on the sensitivity of an immunoreaction test, the surface tension measurements were coupled to an immunoreaction protocol and then to fluorescence measurements for demonstrating that the fluorescence signal decay as the protein agglomerates over the time.

This Ph.D. thesis was structured as reported in the following:

- Chapter 1 *Pyro-electrohydrodynamic jet:* the pyroelectric and the electrohydrodynamic effects were discussed. An overview of the pyro-electrohydrodynamic jet and a description of the optical experimental setup were reported. Moreover, the main results obtained during the years and the multiple p-jet applications were described.
- Chapter 2 *The experimental set-up evolution:* the initial idea of a new p-jet setup configuration for applying the DSS technology was described. The preliminary experimental tests to define the optimal configuration with the best performances were reported. Besides, an alternative configuration of the optical p-jet setup for dispensing droplets with a high rate of deposition was described.
- Chapter 3 *Material and methods*
- Chapter 4 *Results and discussions*
- Chapter 5 *General conclusions and future perspectives*

Chapter 1 An introduction to the "p*yro-electrohydrodynamic jet*"

1.1 Pyroelectric effect

The handling of fluids is realized by using the pyroelectric effect, which is a property of certain crystals that have a spontaneous polarization P_s and can be described as the ability to generate a temporary (pyro)electric field when they are heated or cooled[28]. Specifically, in a condition of constant temperature, each dipole has its orientation, and the total electric dipole moment is zero. On the other hand, when a temperature variation is applied a movement between the atoms arises thus a change in the dipole's strength [29] is shown, and, consequentially, a charge displacement on the material surface is established. Figure 1(a,b) shows the schematic side view of a typical ferroelectric crystal at equilibrium (image above) and under local heating (image below). The crystal at room temperature has the polarization charge balanced by the surface charge from the ambient. The thermal stimulation creates a condition of unbalanced surface charge (Figure 1b) which generates an electric field.

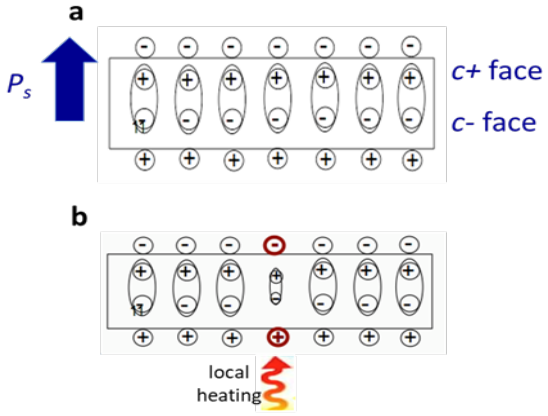

Figure 1. Side view of a ferroelectric crystal: a) at room temperature; b) with a temperature variation, in red circles the transient uncompensated charges that generate a high electric field.

The spontaneous polarization P_s changes according to the following: $\Delta P_i \propto p_i \Delta T$ [30]. P_i is the coefficient of the polarization vector; p_i is the pyroelectric coefficient and ΔT indicates the variation of temperature. At equilibrium, without thermal stimulation, the spontaneous polarization is compensated by the external screening charge and no electric field is present. When the crystal is subject to a temperature variation, a surface charge density $\alpha = p_i \Delta T$ appears locally due to uncompensated charges. Consequently, a high electric field (~10^7 *V/m*) is generated on the surface of the crystal.

1.2 Electrohydrodynamic effect

The electrohydrodynamics (EHD) represents the effect in which liquids emerging from capillary tubes, nozzles, or orifices[31], are subjected to an electric field that is generated by using external electrodes. An electric charge is induced in the liquid, creating electric stress that pulls the liquid in the direction of the field. As a result, due to a charge accumulation at the interface[32,33] a liquid drop assumes a conical shape, called Taylor's cone[34]. Taylor's cone is the result of an equilibrium condition between the forces generated by the surface tension force and the external electric force density[34].

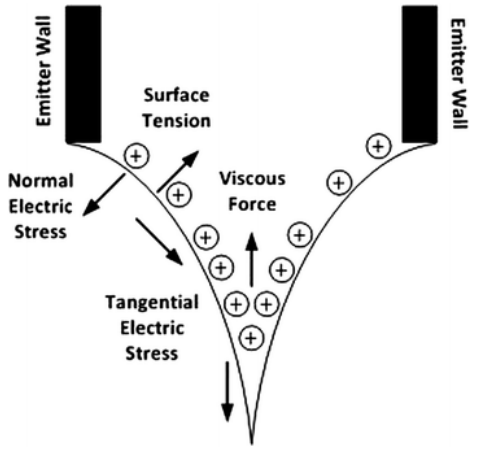

Figure 2. Distribution of charges during Taylor's cone formation.

The EHD has been proposed in the literature for a wide range of applications but still suffers of crucial limitations. For example, it needs the implementation of conductive electrodes on the aperture and on the target surface and the application of high external voltage generators and circuits. Moreover, nozzle clogging[31] issues are often encountered in traditional EHD setups, with detrimental effects in terms of reproducibility. Besides, other disadvantages[35] of this technique are that only solutions/suspensions are processable by using it, the printing on insulating substrates is very challenging and if the potential applied exceeds the substrate could be easily damaged. Additionally, printing is not so repeatable since varies strongly with varying field strength[36–39]

1.3 Pyro-electrohydrodynamic jet

The electric field can be generated by using a pyroelectric crystal (i.e. Lithium Niobate-LiNbO3, LN) so producing the EHD phenomenon. Here the combined effect is called the pyro-electro-hydro-dynamics (pyro-EHD) effect [40]. A pyro-EHD configuration is free from nozzles and electrodes and is based on the use of surface charges generated spontaneously onto pyroelectric crystals[31]. The technique that uses the electric field created by a pyroelectric crystal (i.e. LN), for obtaining separate drops with lower volumes than traditional systems is defined here as Pyroelectrohydrodynamic jet (P-jet) and has been introduced in the literature for the first time by the team where this Ph.D. work was performed [41,42]. Specifically, as shown in Figure 3a**,** the LN is

placed over a microscopic glass cover slide. When heated, the LN generates an electric field, because of which, a liquid droplet, placed underneath the cover slides changes in shape. The liquid droplet evolves into a conical shape under the action of electric, capillary, and viscous forces. As the electric potential increases, the droplet changes in shape into a conic profile (Taylor cone)[31].

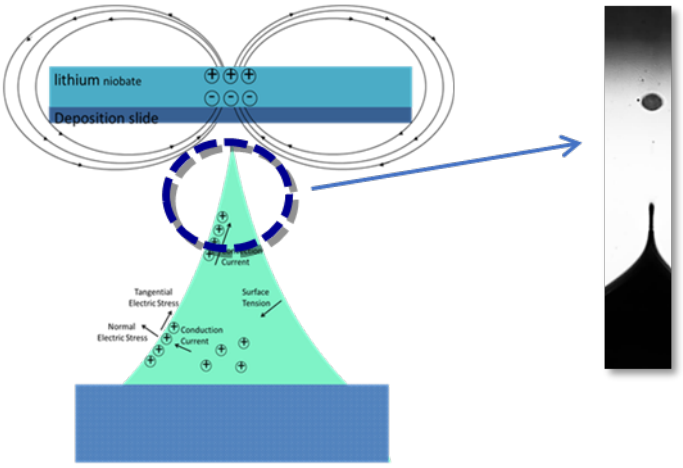

(a) (b)

Figure 3. (a) Schematic representation of the droplet profile evolution when subjected to an electric field, (b) example of a tiny droplet ejected from the Taylor cone tip.

This Taylor conic profile is maintained until a specific threshold of electric potential was reached. Once this critical limit is breached, the meniscus profile can no longer be maintained by the surface tension, and jetting initiates from the Taylor cone tip, which means that several very tiny droplets are produced (see Figure 3b).

1.4 P-jet set-up

Figure 4 shows a schematic representation of the p-jet setup where a CO_2 laser is used for the thermal stimulation.

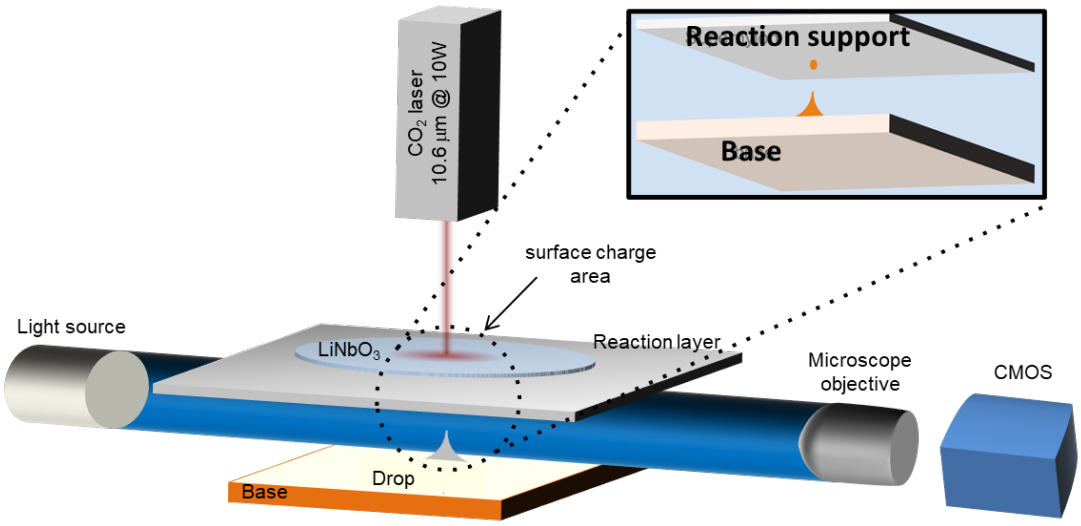

Figure 4. P-jet set-up.

A conventional optical path consists of a collimated LED as a light source, an optical microscope objective (10×), and a high-speed CMOS camera (Motion Pro Y3-S1, pixel size of 10.85x10.85 μm^2). These instruments give a side view during the dispensing events. The p-jet set-up consists of base support where the liquid sample is manually deposited. The liquid sample is called "mother drop" (0.2 µL volume), while the dispensing slide, which represents the reaction layer where the deposition occurs, faces parallel and is mounted on a motorized translation system. The pyroelectric crystal is placed above the reaction layer. Originally, the LN crystal was thermally stimulated by using a laser source that emits in the far-infrared (CO_2 laser, λ = 10.3 µm wavelength falls within the absorption band of the LN crystals)[40,41], then by adopting a conducting wire heater a circulating current produces strictly local heating due to the Joule effect[43].

1.5 P-jet applications

Among the various p-jet applications, the microprinting of different fluids and polymers for soft matter manipulation application[44,45] or for fabricating scaffolds for cells[46] or even the dispensing biomolecules[43,47] are noteworthy. Besides, the p-jet has been used for accumulating low abundant biomolecules, thus significantly increasing the signal-to-noise ratio in fluorescence-based assays. This useful capability was demonstrated in the case of oligonucleotides, gliadin[41], lactose[48,] and collagen[43], by using pre-labelled molecules. The relevant results clearly showed how the (p-jet), has the potential for opening the route to completely new technology for high-sensitive biosensors. The usefulness of a biosensor p-jet based can be extended to any field in which the detection of low concentration quantities is required. For instance, the presence of pathological biomarkers in the blood (currently not detectable with the technologies available on the ticket) suggests the existence of some neurodegenerative diseases such diseases as Alzheimer's disease (AD)[42].

1.5.1 P-jet for liquid dispensing

As mentioned previously the p-jet can print various liquids with different viscosities[31,42]. Usually, dispensing liquids for biochemical analysis or patterning requires the arrangement of appropriate electrodes and the use of high-voltage circuits[40]. The p-jet allows one to print different geometries by controlling the direction of a translation stage and the speed of the deposition slide. So that, the droplets and lines of liquids obtained are highly regular in diameters and widths. Figure 5 shows some simple patterns printed with oleic acid, almond oil, and mineral oil in separate droplets, straight and curved lines.

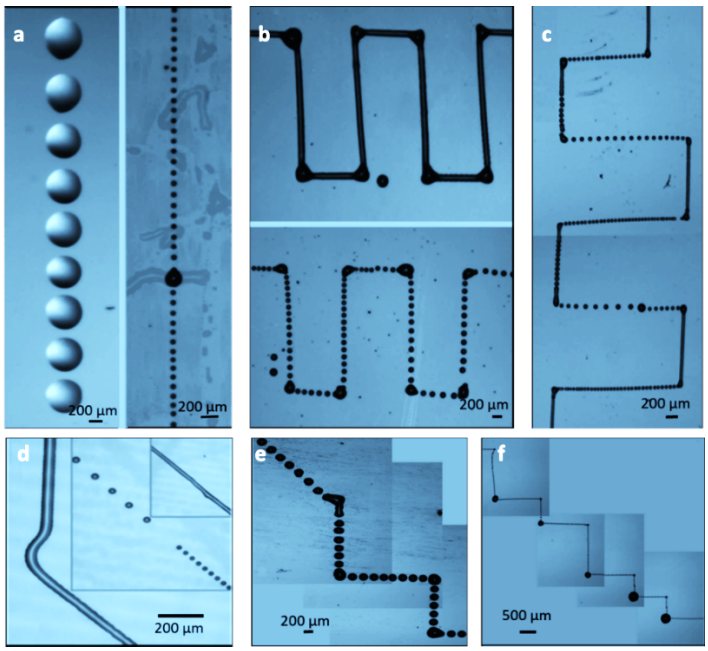

Figure 5. Patterns printed composed of oleic acid, almond oil, and mineral oil in separate droplets, straight and curved lines: a), Linear array of periodic separate droplets printed by almond oil (top) and mineral oil (bottom) (diameter, 15 mm). b) Continuous (top) and dotted (bottom) printed by mineral oil. c) Continuous and dotted patterned by almond oil. d) Simple patterns printed by oleic acid: separate droplets (diameters, 40 and 25 mm), straight and curved lines (width, 40 mm). e) Dotted staircase including a non-orthogonal angle. Staircase with smaller droplets (25 mm) printed with large vertices by almond oil. f), Dotted staircase with small vertices (droplet diameter, 30 mm) printed by oleic acid[40].

The revolutionary feature of the p-jet is to avoid the use of the deposition tools traditionally used in printing protocols (i.e. syringes, nozzles), thus performing much easier and faster dosing procedures[40,42].

1.5.2 P-jet for accumulating biomolecules

The p-jet was presented recently in literature with a perspective application in the field of biosensors[41–43,48]. In fact, the p-jet system can accumulate low abundant biomolecules in tiny droplets directly on the surface of a functionalized slides, thus making them detectable with an improved limit of detection (LOD). The key concept of this type of approach is called “split and stack”[49]. The biomolecules are dispensed on a small area of the deposition slide, and this occurs thanks to the possibility of splitting the mother drop through a series of very small droplets and sticking them in a limited area of the reaction slide.

1.5.2.1 The case of gliadin

The performance of the p-jet for detecting low abundant molecules was tested also in the case of a protein of clinical interest, the gliadin [41]. Gliadin represents the predominant protein component in gluten. The presence of gluten in the food must be kept under control by people with celiac

disease who follow a gluten-free diet. In the European Union, a maximum level of 20 p.p.m. of gluten is allowed for a product declared "gluten-free". To evaluate, the presence of gluten in food is usually used conventional ELISA tests [50]. This technology shows diffusion limits that do not allow the detection of biomolecules when they are in very low concentration. Therefore, a reliable and highly sensitive technique for evaluating the gluten content in foods would be of great benefit to patients, dieters, and food producers. Different concentrations of gliadin labelled by Alexa Fluor 647 (240pg/ml; 120p/ ml; 24pg/ml; 12 pg/ml; 1 pg/ml) were tested. Figure 6a shows the fluorescence signal of the spots obtained with p-jet as a function of the dilution factor of gliadin, while Figure 6b shows the corresponding fluorescence profiles and scanner images of the spots obtained with the p-jet system. The results clearly show that the p-jet system can efficiently detect 1 pg of gliadin in 0.2 µl of solution (0.005 p.p.m.), thus achieving a 60-fold improvement over the current ELISA test limits (0.3 p.p.m.)[51].

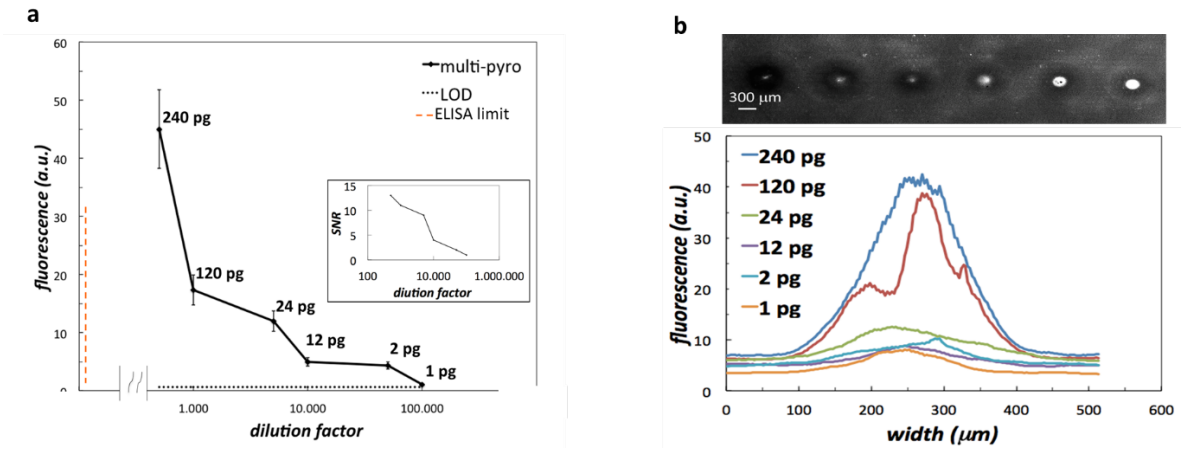

Figure 6. Quantitative evaluation of the gliadin spots. (a) The plot of fluorescence of the gliadins spotted by the p-jet, as a function of the dilution factor and corresponding linearity curve. (b) Mean fluorescence profiles of the gliadins spots obtained with p-jet system and corresponding scanner image where the dilution grows from top to bottom[41].

Chapter 2 *The experimental set-up evolution*

2.1 From the idea to the implementation

This Ph.D. work was focused on the implementation of a new p-jet configuration with additional advantages. The reason behind the set-up optimization was to make it more reliable for biosensing applications. So, the design is expected to modify the p-jet set-up arrangement by ensuring the jetting in the direction from up to down to facilitate the clinician who must directly interface with the system. The process of bioaccumulating in this new, vertically flipped configuration of the p-jet set-up, was allowed with an approach that we defined as “split and stack”. Figure 7 depicts the “split and stack” idea.

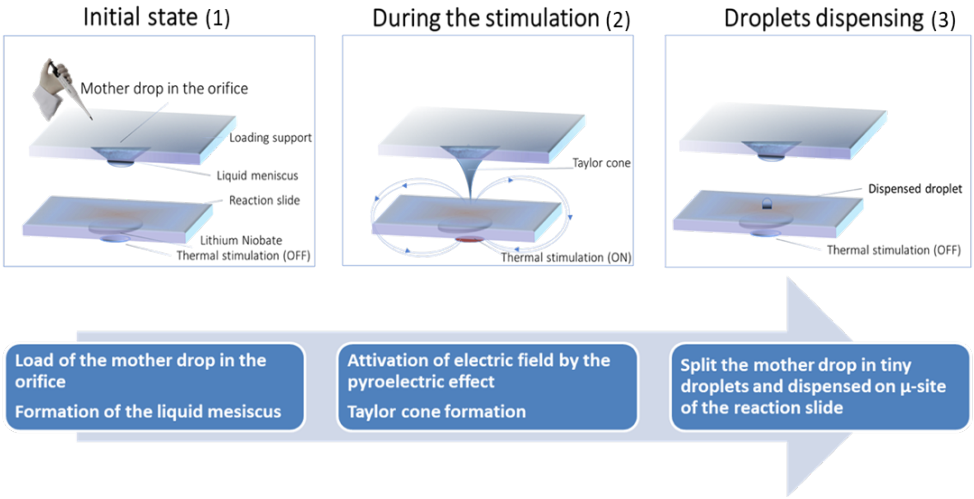

Figure 7. A simplified view of the p-jet system and representation of the droplet split and stack idea.

Specifically, by using a traditional pipette, a droplet (0.5-1 µl in volume) of fluid containing low abundant biomarkers is loaded, into the so-called loading support (LS). The LS is thoroughly described in the following section 2.2. The droplet is forced to pass through an orifice (1) of the LS and, under the influence of the pyroelectric field, generates tiny droplets, as shown in (2) and (3) of Figure 7. The pyroelectric field is created by thermally stimulating the LN (2) with a thermal system (see section 2.3). Because of the stacking of these droplets in a very confined area (hence the name split and stack), the biomolecules are layered on top of each other and bioaccumulated. Successive tiny droplets can be accumulated on a single spot to enhance the number of molecules per unit area of reaction, by keeping fixed the position of the reaction slide. A series of different spots is obtained simply by translating the slide horizontally to a new position. Facilitating bioaccumulation, when the concentration of biomarkers in the sample is very low, is the key to early disease diagnosis.

2.2 The loading support

The LS is a part of the p-jet set-up in which an operator loads a droplet of a biological sample by using a traditional pipette. Specifically, the LS is a Poly-methyl methacrylate (PMMA) slab characterized by an orifice with a conical shape. Figure 8 shows a picture of the LS.

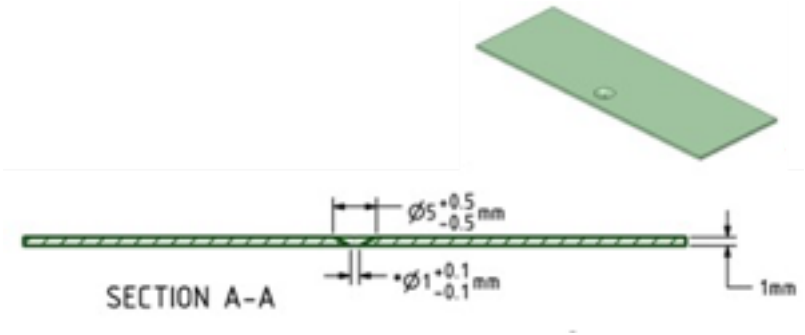

Figure 8. Side view of the LS.

It has been realized by the Vrije Universitate Brussel (VUB) in cooperation with the National Research Council (CNR). CNR defined the requirements and geometrical dimensions for the orifice in the loading support, and then VUB fabricated it according to the desired features. The appropriate orifice should be able to generate tiny droplets with repeatable volume and ejection speed.

2.2.1 Determination of the loading support geometrical features

The evaluation of suitable geometrical parameters of the LS was determined by modelling the dynamics of a water drop passing through a channel (or orifice). This task was carried out by Professor Maffettone's research group at the Department of Chemical, Materials and Production Engineering University of Naples Federico II in collaboration with CNR. Specifically, the values of orifice inclination angle (α), bottom radius (r), and height (H) were defined. In particular, the simulations identified the orifice profile that allowed the formation of a relatively thin pending meniscus, with a thickness of around 100 μm. A numerical mesh was defined by adopting the geometry reported in Figure 9.

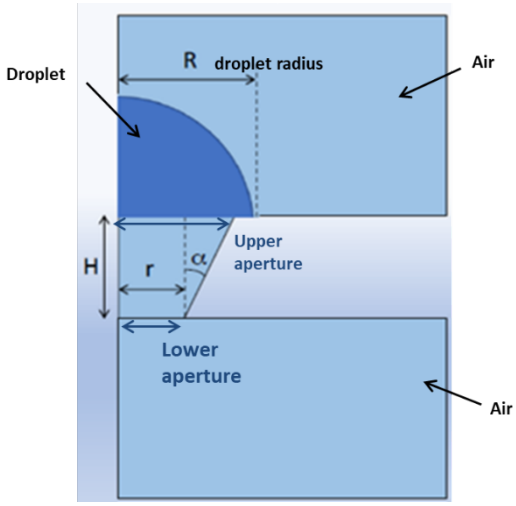

Figure 9. Schematic view of the geometry adopted in the simulations.

Volume-Of-Fluid (VOF) simulations in OpenFOAM were performed to study the meniscus formation. OpenFOAM (Open Field Operation And Manipulation) is a C++ toolbox for the development of customized, and pre-/post-processing utilities for the solution of continuum mechanics problems, most prominently including computational fluid dynamics (CFD). In the VOF method the transport equation (1) for the volume fraction of one phase is solved simultaneously with the continuity (2) and momentum equations (3):

$$\frac{\partial \alpha}{\partial t} + \boldsymbol{\nabla} \cdot (\boldsymbol{U}\alpha) = 0 \quad (1)$$

$$\boldsymbol{\nabla} \cdot \boldsymbol{U} = 0 \qquad (2)$$

$$\frac{\partial (\rho \boldsymbol{U})}{\partial t} + \boldsymbol{\nabla} \cdot (\rho \boldsymbol{U}\boldsymbol{U}) = -\boldsymbol{\nabla} p + \boldsymbol{\nabla} \cdot \boldsymbol{T} + \rho \boldsymbol{f_b} \qquad (3)$$

where **U** represents the velocity field shared by the two fluids throughout the flow domain, α is the phase fraction, **T** is the deviatoric viscous stress tensor {**T**=2μ**S**-2μ(**∇**·**U**)**I**/3 with the mean rate of strain tensor **S**=0.5[∇**U**+(∇**U**)^{T}], and **I**≡δ_{ij}}, ρ is density, *p* is pressure, and $\boldsymbol{f_b}$ are body forces per unit mass (gravity and surface tension effects at the interface). In VOF simulations the latter forces include gravity and surface tension effects at the interface. A relevant parameter is the phase fraction α which can take values ranging from 0 to 1 ($0 \leq \alpha \leq 1$), where 0 and 1 correspond to regions accommodating only one phase, e.g., α=0 for gas and α=1 for liquid. Accordingly, gradients of the phase fraction are encountered only in the region of the interface. To solve the differential equations, the software requires the following boundary conditions:

- Outflow on the outlet boundaries
- Axial symmetry on the axis of symmetry
- Slip with a prescribed contact angle on the walls

Two immiscible fluids are considered as one effective fluid throughout the domain, the physical properties of which are calculated as weighted averages based on the distribution of the liquid volume fraction, thus being equal to the properties of each fluid in their corresponding occupied regions and varying only across the interface

$$\rho = \rho_l\gamma + \rho_g(1 \quad -\gamma)\mu = \mu_l\gamma + \mu_g(1-\gamma) \quad (5)$$

in which ρ_l and ρ_g are the densities of liquid and gas phases. One of the critical issues in numerical simulations of free-surface flows using the VOF model is the conservation of the phase fraction. This is especially the case in flows with high-density ratios, where small errors in volume fraction may lead to significant errors in calculations of physical properties. Accurate calculation of the phase fraction distribution is crucial for a proper evaluation of surface curvature, which is required for the determination of surface tension force and the corresponding pressure gradient across the free surface. The interface region between two phases is typically smeared over a few grid cells and is therefore highly sensitive to grid resolution. VOF simulations have been made for a water drop initially spherical in an air domain. The physical parameters for the two phases necessary to solve the problem are reported in Table 1.

PHISYCAL PARAMETERS (water/air system)	
Drop Viscosity	0.001 Pa*s
Drop Density	1000 Kg/m^3
Surface tension	0.07 N/m
Contact Angle	60°
Air Density	1 Kg/m^3
Air Viscosity	1.48* 10^{-5} m^2/s

Table 1. Physical parameters of the water/air domain.

Finally, ParaView was used for visualizing the resulting data. Figure 10 shows a typical output of ParaView with an indication of the region corresponding to what we call “meniscus thickness” here.

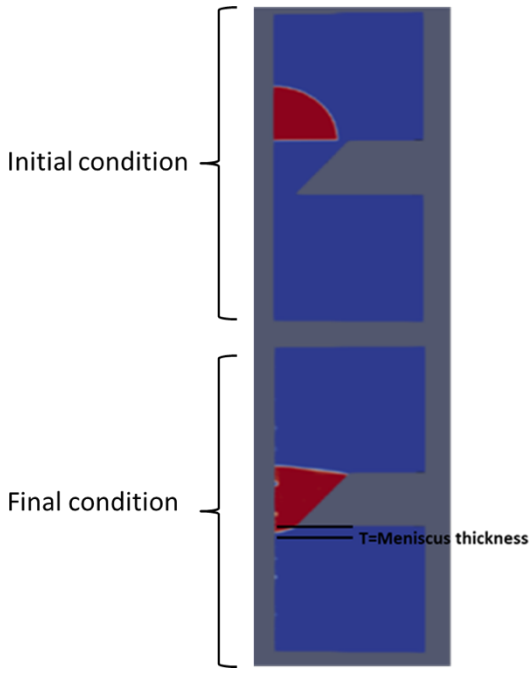

Figure 10. Typical output of ParaView with an indication of the region corresponding to what we call “meniscus thickness” here.

The upper row shows the initial condition, whereas the bottom row refers to the final configuration once a steady state is attained. **Table 2** summarizes the three conditions that have been simulated here.

PARAMETER	Condition 1		Condition 2		Condition 3	
r	0.5 mm	fixed	1 mm, 0.5 mm	variable	0.5 mm	fixed
H	1 mm	fixed	1 mm	fixed	1 mm, 1.5 mm	variable
□	1°, 5°, 10°, 20°, 30°, 40°	variable	40°	fixed	40°	fixed

Table 2. Summary of parameters that have been changed during simulations.

In each of the three conditions one of the following parameters is variable:

1. Orifice inclination angle (α)

2. Orifice bottom radius (r)

3. Orifice height (H)

- Condition 1: Variable orifice inclination angle (α)

The LS with μ-orifice represents the part of the sensor interfacing the operator who will have to load the drop of a biological sample. As mentioned before the shape of the μ-orifice has to facilitate as much as possible during this loading step. A conical shape with the upper aperture larger than the lower aperture would facilitate the above-mentioned loading step. Figure 11 reports the snapshots corresponding to the initial (upper row) and the final (lower row) states for a variable value of α.

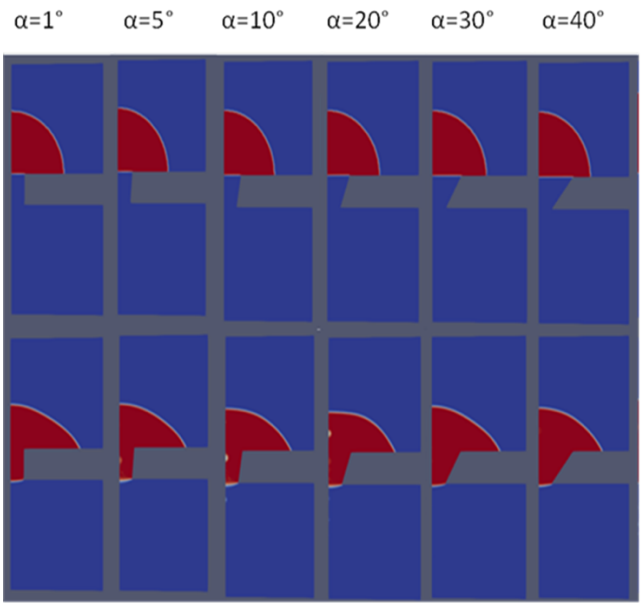

PARAMETER	VALUE	
r	0.5 mm	fixed
H	1 mm	fixed
α	1°, 5°, 10°, 20°, 30°, 40°	variable

Figure 11. Initial (upper row) and final (lower row) ParaView snapshots for a drop-through orifice with r=0.5mm, h=1mm, and an increasing α.

The numerical results provide no significant variations for the meniscus thickness, which remains around 100 μm for all the inclination values, with a percent variance of 20 %. Therefore, according to the above-mentioned need for a larger upper aperture, the inclination angle at 40° was fixed.

- Condition 2: Variable orifice bottom radius (r)

Once fixed the inclination angle (α), the behaviour of the meniscus thickness by varying the orifice bottom radius (r) was investigated. Figure 12(a,b) shows the final snapshots for the steady-state of a drop-through two orifices with r=1 mm and r=0.5 mm, respectively. The values of H and α fixed at 1 mm and 40°, as indicated in the table alongside.

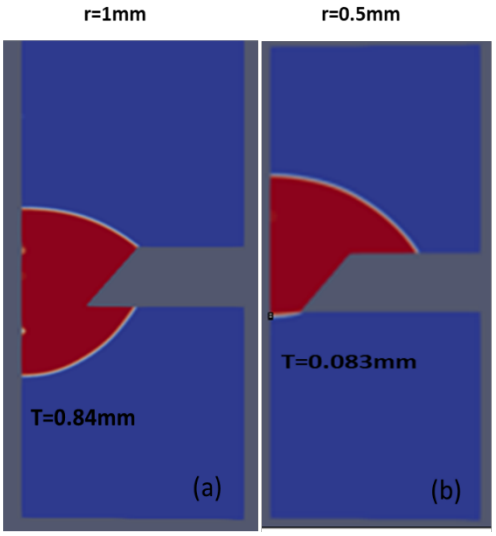

PARAMETER	VALUE	
r	1 mm, 0.5 mm	variable
H	1 mm	fixed
α	40°	fixed

Figure 12. Final snapshots for the steady-state of a drop exiting two orifices with (a) r=1mm and (b) r=0.5mm.

The simulation generates a meniscus thickness of around 800 µm and 80 µm in cases of r=1 mm and r=0.5 mm, respectively. Therefore, the value of the lower aperture radius to r=0.5 mm was fixed.

- Condition 3: Variable orifice height (*H*)

Figure 13 shows the results obtained in the case of a variable orifice height (*H*).

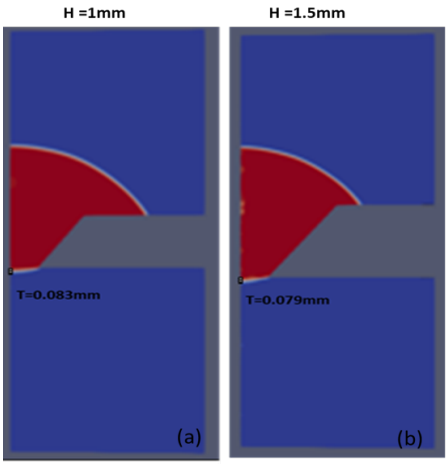

PARAMETER	VALUE	
r	0.5 mm	fixed
H	1 mm,1.5 mm	variable
α	40°	fixed

Figure 13. ParaView snapshots corresponding to the steady-state for a drop-through orifice with r=0.5mm, α=40°, where (a) is related to H=1mm and (b) to H=1.5mm.

These results demonstrate the irrelevance of the orifice height (*H*) for the meniscus thickness in the range of values investigated here. This allows us to use thicker loading support in case of stability and rigidity needs arising during the experimental implementation. As a result, for the realization of the loading support, an upper limit value for the lower aperture radius *r* of 0.5 mm was considered. Indeed Figure 12 shows that a bottom orifice radius *r*=1 mm leads to the worst scenario: liquid generating a meniscus with a thickness ~10-fold larger than the target value of 100 um. With this in mind, VUB fabricated the LS with the characteristics listed in Table 3.

Inclination, α [=]°	**Thickness, H [=] mm**	**Bottom Diameter, D_b [=]mm**
40	1	≤ 1

Table 3. Geometric characteristics of the first batch of loading support fabricated by VUB.

2.3 The heating system

Rather than adopting the CO2 laser head or the □-heater used in our first papers mentioned above, a heating system that is more compact and easier to use has been developed. Here, the LN was heated for generating the pyroelectric effect by using an external heater made of a tungsten wire (TW). Figure 14 shows the side, top, and bottom views of the heater.

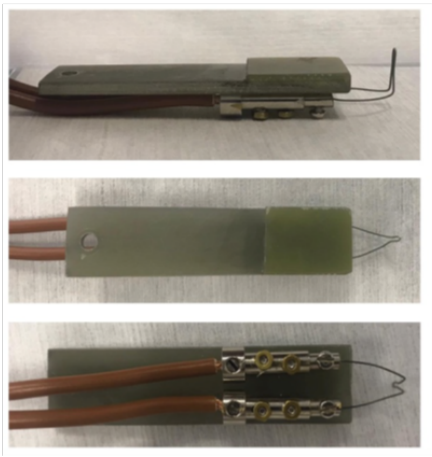

Figure 14. Sideview, top, and bottom of the heater.

The wire is heated by the Joule effect at regular time intervals, by applying a simple step function through a voltage generator, Figure 15 shows the main parts of the heating system.

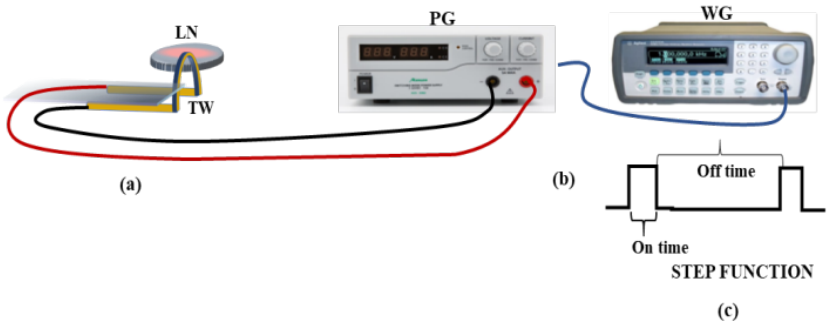

Figure 15. simplified view of the circuit driving the heater, consisting of a power generator (*PG*) and a waveform generator (*WG*) modulated by TTL signal. *LN*, lithium niobate; *TW*, tungsten wire.

A conventional TW 300 µm thick was bent appropriately to get a nearly point-wise heat source in contact with the LN crystal (see Fig. 15a). The thermal stimulus was controlled by the power dissipation in the TW driven by a power generator (PG). The waveform generator (WG) allows for the generation of electrical waveforms and Figure 15b represents the simplified view of the circuit. The step function indicated schematically in Figure 15c was used, where the 'on' and 'off' times corresponded to the time-lapse in which the current passed or did not through the TW, correspondingly. It is well known that a temperature value exceeding 37°C is detrimental to biomolecules. Therefore, the temperature of the surface of the target slide was measured by an infrared camera under different values of voltage and on/off times, to find the conditions that produce repeatable jets, but at the same time respect the limit of temperature. Table 4 reports the setting parameters that were defined downstream of the tests.

Voltage, V	ON time, s	OFF time, s	TOTAL time, s
1.7	3.5	56.5	60

Table 4. Setting parameters of the step function applied to the heating wire.

The LN crystal heats up to 35°C in about 15 s, when subject to the heating step, and cools down to room temperature in about 15 s, as observed by a standard thermal imaging camera. This cycle of temperature variation generates the pyroelectric effect, and the intensity of the resulting electric field is high enough to induce a charging effect on the free surface of the liquid meniscus on the pin. The charged surface experiences a Coulomb repulsion, which overcomes the surface tension of the liquid up to the release of a liquid jet. Three jets were produced on average during one heating step. It is possible to apply different pulses to produce the desired number of jets. Each ejected droplet is observed sideways by a standard camera (Motion Pro Y3-S1, IDT Corporation, pixel size of 10.85×10.85 µm) and contains around 1 nL of solution on average.

2.4 Preliminary experimental tests

Once VUB realized a first batch of LSs and the heating system was optimized, preliminary tests were done on the LSs, which have different dimensions and different surface properties. Keeping in mind that the foremost goal of the p-jet sensor is to trigger sequences of tiny droplets well-repeatable in volume and diameters, multiple tests to achieve these aims were performed. Specifically, the LSs, listed in Table 5 realized by VUB, with different bottom diameters were investigated.

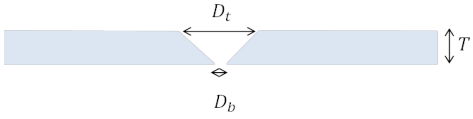

Top diameter, mm (D_t)	Thickness, mm (T)	Bottom diameter, mm (D_b)
5	1	1.02
		1
		0.88
		0.62

Table 5. Geometrical characteristics of the LSs fabricated by VUB.

P-jet tests were carried out with different mixing buffers (see Table 6) to investigate the effect of the surface tension on the ejection of droplets with reduced diameter compared to water-based samples. The LS with D_b of 0.62 mm was used. Figure shows the side view of the corresponding droplet ejection. Table 6 reports the liquid samples which were tested.

SAMPLES			
		β-amyloid concentration [=] µg/ml	**Labels**
1	β-Amyloid in distilled water	50	dH_2O
2	β-Amyloid &Triton 0.04% solution	50	Triton 0.04% solution
3	β-Amyloid &Tween 0.04% solution	50	Tween 0.04% solution
4	β-Amyloid &Tween 10% solution	50	Tween 10% solution
5	β-Amyloid & Glycerol 10% solution	50	Glycerol 10% solution
6	β-Amyloid & DMSO 1% solution	50	DMSO 1% solution

Table 6. Liquid samples were tested.

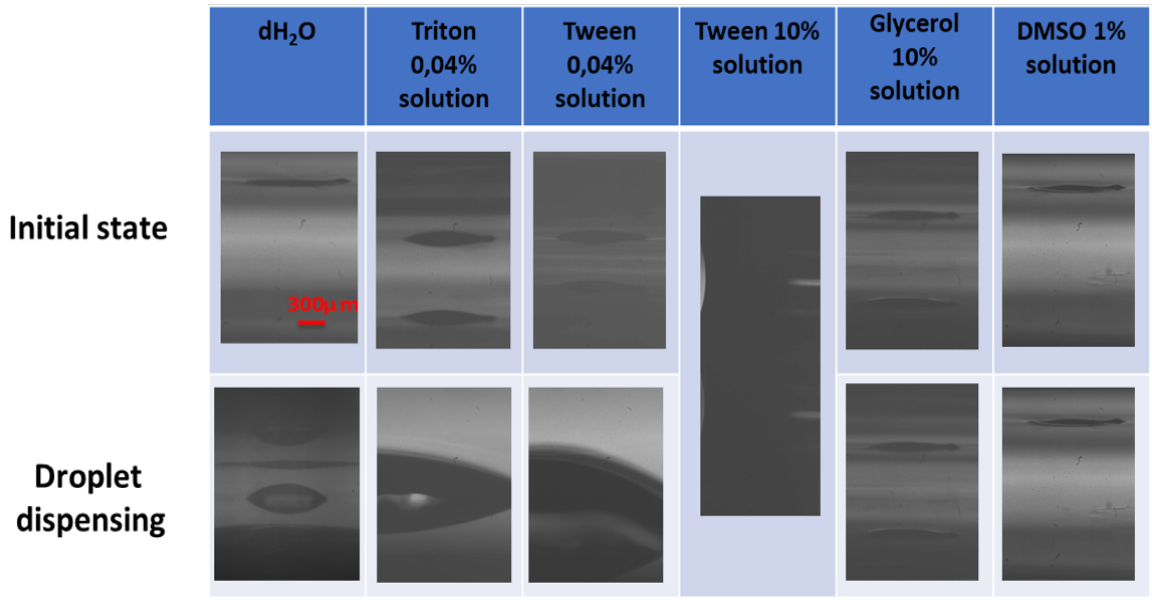

Figure 16. Experimental results, initial and final snapshots of the results of the experiments.

The upper row shows the side view (Camera Motion Pro Y3) of the liquid meniscus pending from the orifice, while the lower row shows the typical droplet deposited after activating p-jetting through the thermal stimulation of the LN slab. Regardless of the solutions tested, a fast emptying of the orifice or larger diameter of the droplet dispensed were obtained. Moreover, the LS with a larger bottom diameter (1mm; 1.02mm; 0.88mm) produced droplets with diameters even larger, and, considering their lack of significance for the aims of the thesis, the related data are not reported here for brevity. Despite these first results, the attention was focused on other LSs with lower D_b as well as on their wettability, which was enhanced with Plasma Treatment. Thus, we carried out additional tests with this second batch of LSs fabricated by VUB reported in Table 7.

Top diameter, mm (D_t)	Thickness, mm (T)	Bottom diameter, mm (D_b)	Plasma Treatment
5	2.8	0.46	yes
		0.36	yes
		0.32	yes
		0.44	no
		0.35	no
		0.29	no

Table7. Geometrical characteristics of LSs second batch fabricated by VUB.

Figure 17 shows the side view images of the typical droplet dispensing in the case of the orifices with Db=0.32 mm and 0.29 mm.

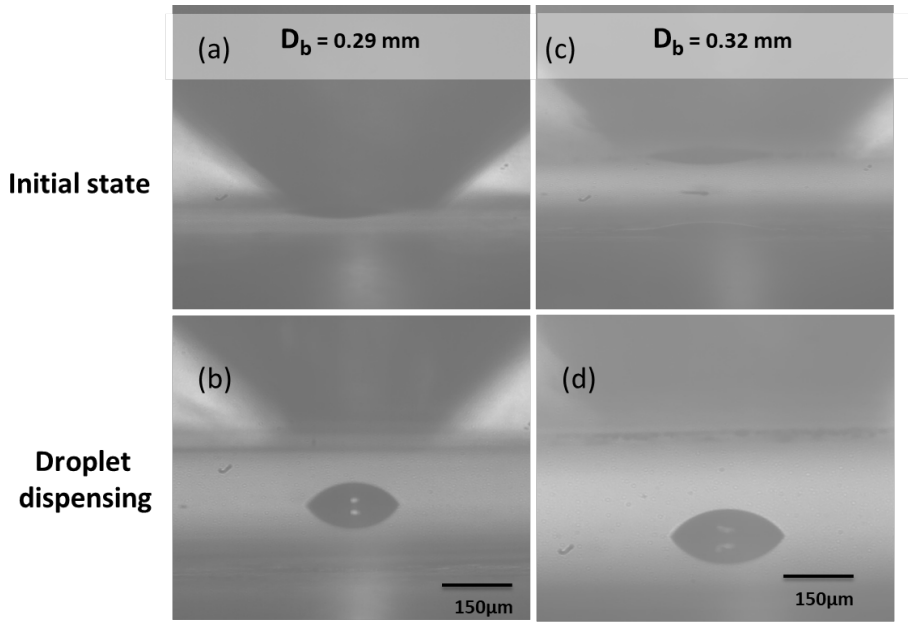

Figure 17. Meniscus formation and droplet deposition for orifice diameter equal to (a)-(b) 0.29 mm (c) - (d) 0.32 mm.

Although the droplets dispensed had smaller diameters (i.e. around 250 µm), these (for both treated and untreated plasma orifices) were not repeatable. Besides, the strict dependence of the droplet's diameter dispensed on the D_b was verified. The orifices with the biggest dimensions have not shown good results due to the fast emptying of the orifice and the large diameter of the drop dispensed.

2.5 The orifice-pin configuration

Due to the unsatisfied results achieved, an alternative configuration of the LS was tested. This new configuration was characterized by the loading support with a printing pin (described in subsection 2.5.1) inserted into the orifice with a bottom diameter of 1 mm. The aim was to achieve a more pointed liquid meniscus and, consequently, a more accumulated charge on its apex to shorten the

diameter of the ejected droplet and improve its repeatability. Figure 18a shows the orifice slab together with a frame used for fixing the pin, while Figure 18b shows the loading support with the orifice-pin configuration.

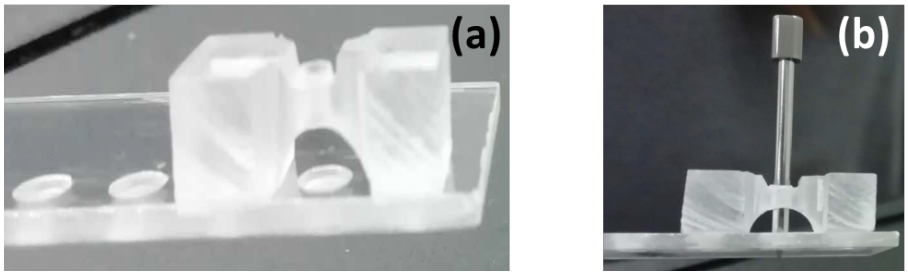

Figure 18. Pictures of (a) the orifice with frame and (b) the loading support with orifice-pin configuration.

2.5.1 The printing pin

The pin is a commercial microarray stealth printing pin (SMP3, Arrayit Corporation) usually employed for contact printing of microarray slides[52]. Figure 19(a,b) show two optical microscope images of the pin at different magnifications, while Figure 19(c) shows a sketch of the pin tip, with the characteristic dimensions. Here, for the first time, an electric field for drawing tiny droplets from the pin, avoiding contact on the slide was used.

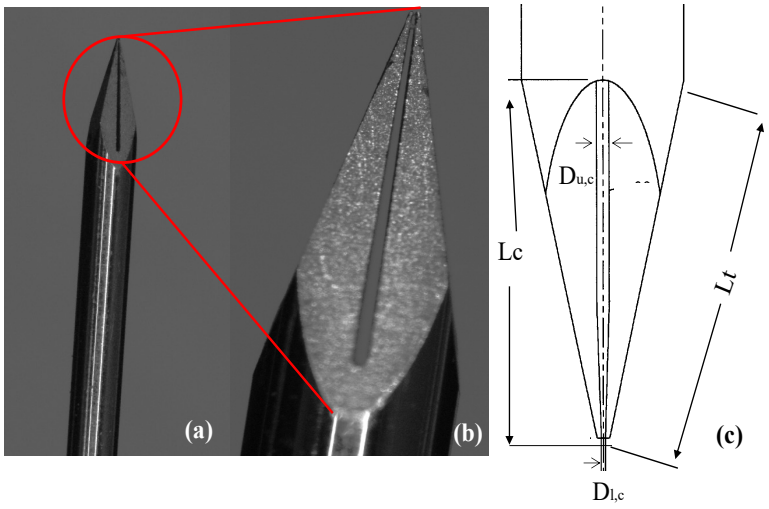

Figure 19(a,b). Optical microscope images of the printing pin at different magnifications; (c) sketch of the pin tip, where $D_{l,c}$ = 20 µm, $D_{u,c}$ = 105 µm, L_c = 2 mm, L_t = 2.3 mm.

The commercial printing approaches are usually classified as contact and non-contact printing. Contact printing typically uses a pin, which is usually designed from stainless steel, titanium, or tungsten. Contact printing has several drawbacks such as the deformation of the tip, which introduces imprecision about deposition[53–55], or the contaminations of the biological samples. Conversely, the non-contact printing heads, such as those based on piezoelectric nozzles, eject the sample droplets from a specific distance[56], thus avoiding contact-related issues. However, failed

spots, satellite spots, and misplaced spots[57] may occur in this modality. Here, the outstanding novelty in the use of pin is that the ejection of tiny droplets from the capillary of the stealth pin is achieved through an electrostatic interaction at short distances, thus preserving the spatial precision of contact printing, but at the same time avoiding the typically related drawbacks.

2.5.2 The new p-jet configuration

Figure shows the two instants of the p-jet achieved by using the microarray pin.

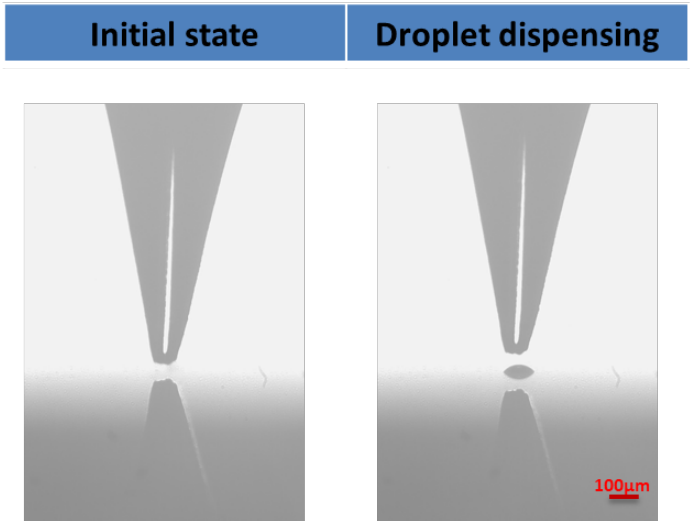

Figure 20. Optical microscope side view of the p-jet through the orifice-pin configuration. Left: initial state. Right: droplet deposition.

To verify the repeatability of the spots obtained through the orifice-pin loading support, a fluorescent probe (Alexa 647 with a dilution rate of 1:200 in water) was tested by depositing one jet for each spot. The dispensing has proven to be fast (one second for each drop dispensed) and with droplets diameter which is around 100 µm. Tests were successful in obtaining 20 spots with high repeatability in terms of diameter and fluorescence intensity as shown in Figure 21.

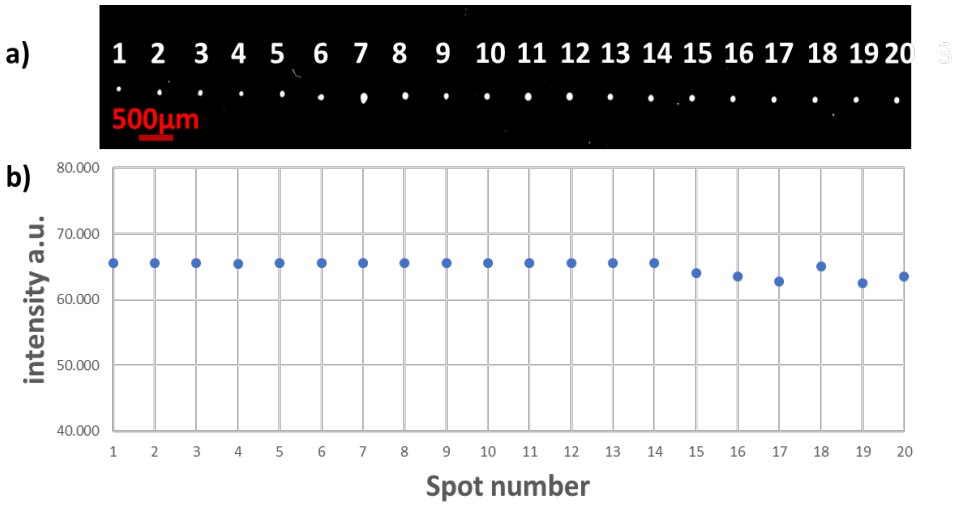

Figure 21. (a) Typical scanner image of replicates of p-jet spots on a glass slide. (b) Distribution of the fluorescence intensity over the replicated spots shown in (a).

As a result, the orifice-pin configuration (see Figure 18b) was selected for the successive experiments. The optical path for inspection of droplet formation was kept fixed as reported in section 1.4, while the dispensing part was changed by adopting the orifice-pin configuration (see Section 2.5) and the thermal stimulus described in Section 2.3 for thermally stimulating the LN crystal and generating the pyroelectric effect. Figure 22 schematic depicts the new p-jet configuration.

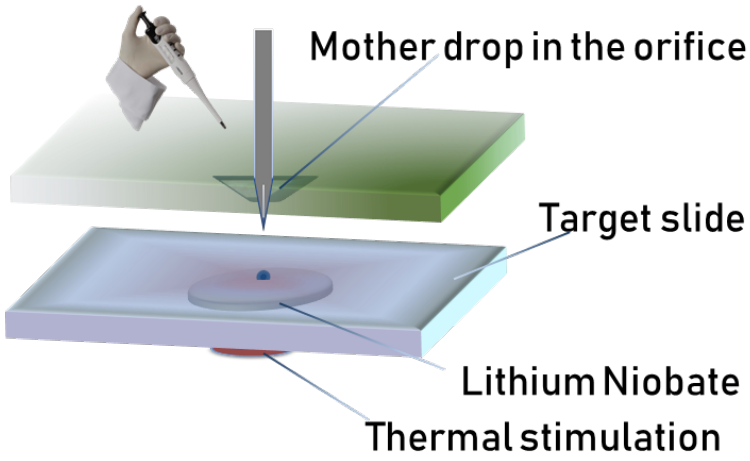

Figure 22. Schematic view of the new p-jet configuration developed in this thesis work.

2.6 The p-jet set-up for high-rate accumulating tiny droplets

During this thesis work another p-jet configuration was tested with the aim at achieving an high-rate accumulation of tiny aqueous droplets, through a single thermal stimulation. As shown in the following, in this configuration an appropriate heating ramp is applied on a small piece of LN crystal[58]. The liquid sample is loaded into an orifice from the top (analogously to the scheme in Fig.22 but without the pin), thus improving significantly the very first procedures where a crucial deposition in the form of a sub-μL mother drop was needed[40,41,43]. The ability of this proposed p-jet configuration to accumulate about 70% of the dispersed aqueous droplets into a limited area with a micrometric cross size was proved. Figure 23 shows a schematic view of the top-down configuration of the p-jet used for achieving a high-rate accumulation of tiny aqueous droplets ejected from a liquid's meniscus.

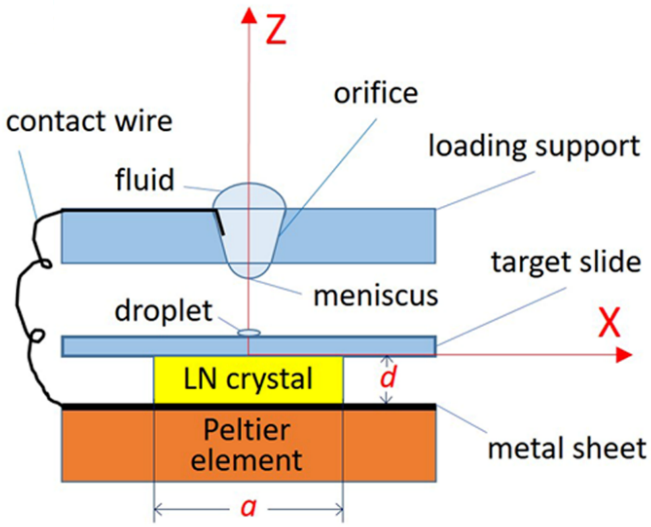

Figure 23. Schematic view of the top-down p-jet configuration where the *XZ* coordinates, and the crystal dimensions refer to the simulation model indicated later.

The aqueous sample (around 10 μL) is loaded into the orifice of the LS (for more details about LS see paragraph 1.1) by using a standard pipette. The LS was positioned at around 300 μm from the top surface of the target slide. Once the orifice is filled with the liquid sample, a stable meniscus emerged as shown in Figure 23(a). A standard XYZ micrometric manual translation stage is used for aligning the orifice aperture with the central point of a square piece of LN crystal. Both sides were polished and z-cut wafers of monodomain LN with 0.5 mm thickness and 3-inch-diameter were bought from Crystal Technology Inc. To obtain LN samples with a thickness of 1 mm, two cleaned LN plates with a thickness of 0.5 mm with the same lateral dimensions and polarization direction were stacked up and glued together with standard thermal paste. The target slide, which was the slide were accumulating the tiny droplets, is a commercial SuperAmine 2 slide usually used for binding biomolecules (SMM2, ArrayIt®) and is inserted between the orifice and the LN crystal. The slide was 75x25 mm^2 sized and 1 mm thick. The heating element underneath the crystal belongs to a commercial heating plate (Linkam) or a standard Peltier element 15x15 mm^2. The Peltier element was 15x15 mm^2 large and was driven by a stepwise current pulse of 0.5 A (with 0.6 V voltage) provided by a programmed power supply HCS-3300, to raise the crystal temperature from 25°C up to about 40°C. As represented in the figures, a thin metal wire is inserted into the orifice, which is put in contact with the liquid and a thin metal sheet between the crystal and the heating element, to ensure electrical neutralization of the meniscus after the emission of a charged droplet and to enhance the electric field strength. The droplet ejection started 7 s after Peltier powered on and finished after about 46 s when the electric field decreased. All droplets were deposited within a target slide area with a diameter of about 150 □m. A video at a 50 fps frame rate was recorded by using an optical path composed of a LED source, a microscope objective, and a PC-controlled camera. The images of the recorded movie were analyzed for evaluating quantitatively the rate of

accumulation of the droplets on the target slide. The events of droplet deposition are illustrated in Figure 24 which presents the frames extracted from the Movie. Figure 24b and 24d correspond to the deposition of the first and second droplets, and Figure 24a and xc - frames preceding these events, respectively. Figure 24e shows all deposition events of individual droplets versus time, represented by peaks with a height equal to the droplet volume V, expressed in picolitres. The figure demonstrates that 92 jets of individual droplets were identified within approximately 14 seconds, while 14 multiple (2-3) droplet ejection events were excluded from the analysis. A time interval between two adjacent jetting events ranges from 0.10 to 0.66 s. Droplet volumes range from 5 to 25 pl with an average of 14 pl and a standard deviation of 4.8 pl.

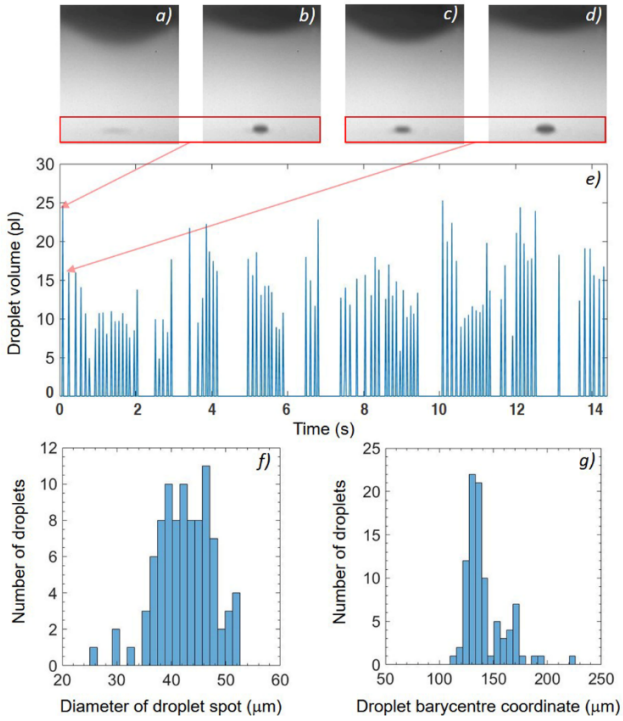

Figure 24. b,d) Frames from the movie corresponding to deposition events of the first and second droplets, respectively. a,c) Frames preceding these events, respectively. e) Droplet deposition events as a function of time, represented by peaks with a height equal to the droplet volume, where the red arrows indicate the first and second droplet deposition events. f) Histogram for the distribution of a diameter of the area which can be covered by the individual droplet. g) Histogram for the distribution of the droplet barycenter coordinate.

The following analysis aims at estimating how many droplets overlap on the restricted area of a target slide. Therefore, the diameter of the area that each ejected droplet with a known volume V can cover was determined. The diameter of the covered area (here we call this area a “droplet spot” for brevity) was calculated on the assumption that a deposited droplet has a 74 ° contact angle with the target slide surface and forms a spherical interface with air. The histogram in Figure 24f shows the frequency distribution for a droplet spot diameter. The mean value of a droplet spot diameter D_{mean} was 42.5 μm. A barycenter coordinate of the deposited droplets was determined by using a standard procedure integrating the grey levels of the pixels. The histogram of the frequency

distribution of the barycenter coordinate is plotted in Figure 24g. The histogram demonstrates that 74 droplets have the barycenter coordinate in a region about 40.6 μm wide, which is less than D_{mean}, and so the droplet spots overlap at least partially within this region. This can provide an approximately 70-fold increase in the surface density of the analyte molecules dissolved in the aqueous sample compared to the deposition of a single drop. So, this new p-jet configuration can produce a pyroelectric field which allowed us to achieve a high-rate accumulation of tiny aqueous droplets in a single thermal stimulation. Specifically, this p-jet configuration was successful in obtaining an accumulation of more than 70 tiny aqueous droplets during the first 14 seconds on the target area with a diameter of less than 40 μm. As a result, this technique could open the route to easy accumulation of biomolecules for high-sensitive detection of highly diluted biomarkers.

Chapter 3 *Materials and methods*

3.1 Lithium niobate and the pyroelectric effect

Lithium niobate (LN) is a rhombohedral crystal that was bought from Crystal Technology Inc. in the form of both sides polished 500 m thick c-cut 3-inch wafers. The wafers were cut into 2 cm^2 sized samples by a standard diamond saw. The spontaneous polarization Ps of the LN crystal changes according to $\Delta P_s = p\,\Delta T$, where p is the pyroelectric coefficient and ΔT is the temperature variation ($p = -8.3 \times 10^{-5}$ C m^{-2} K^{-1} at T=298 K). At thermal equilibrium, the spontaneous polarization of the crystal is completely screened by the external charges accumulated on the crystal surfaces and no electric field is present. When the crystal is stimulated through a temperature variation, an uncompensated surface charge density $\sigma = \Delta P_s$ and electric potential difference $\Delta U \sim \sigma d/(\varepsilon_0 \varepsilon)$ appear on the crystal surfaces (here d is crystal thickness and ε_0, ε are dielectric constants of vacuum and of the crystal, respectively). This potential difference can reach 10^4 V for mm-sized crystal thickness and ΔT of about 10 K.

3.2 Reaction slide

In the case of the fluorescent probes, we used standard 1 mm thick microscope glass slides, without specific surface functionalization. Whereas for the immunoassay application, we used glass slides functionalized with 2D-Amine groups (PolyAn GmbH, Germany) and with a standard size of 25 × 75 × 1 mm. In this case, the surface is functionalized by NH_3^+ groups for non-covalent coupling of negatively charged biochemical species via electrostatic adsorption.

3.3 Fluorescent probes

Two kinds of fluorescent probes were used: the Alexa Fluor 647 fluorophore, a far-red-fluorescent dye (cat. no. A33084, life technologies), and a secondary antibody conjugated with a fluorophore, the Alexa Fluor Plus 647 (cat. no. A32733, life technologies). The fluorophore was bought as a powder and dissolved in 1X Phosphate Buffered Saline (Life Technologies Cat.N. 10010023), at a concentration of 1.25 mg/ml, the solution was mixed gently to ensure the solubilization of the powder. Starting from this solution, 20 µl, 9.6 µl, and 5 µl were diluted in 2 mL of PBS (Phosphate-buffered saline) 1X, each one, to have the final concentrations of 12.5 µg/mL, 6 µg/mL, and 3 µg/mL. The secondary antibody was bought as a solution with an initial concentration of 1 mg/mL and diluted in dH_2O at the final concentrations of 10 pg/mL, 0.1 pg/mL, and 0.01 pg/mL.

3.4 Aβ1-42 protein solution

The technique was tested for a biomarker of clinical interest, the Alzheimer's A1-42 protein (Sigma Aldrich AG912). The white lyophilized powder was resuspended in 1% Ammonium hydroxide solution (NH_4OH) (Sigma-Aldrich 221228) at a concentration of 1mg/ml according to manufacturing procedures, sonicated for 30 seconds, and stored undiluted at -20°C. The serial dilutions were prepared with PBS1X to obtain the final concentrations of 100 pg/mL, 20 pg/mL, and 4 pg/mL.

3.5 Immunoreaction protocol

The Aβ1-42 was deposited by using the p-jet system, afterwards, the slide was incubated in a humid chamber for 2h at 25°C. For saturating excess protein-binding sites, the slide was covered with 2mL of ArrayIt Blocking solution (BlockIt Blocking buffer) for 1h at 25°C. The blocking solution was used to dilute the antibody solutions. Then the slide was washed by placing it in a Petri dish with 10mL of PBS 1X (Gibco 10010023) for 2 minutes. This washing cycle (WC) was repeated three times. A solution of primary antibody (Ab), 2mL of rabbit anti-β-Amyloid 1-42 (CellSignaling Technologies Rabbit D9A3A) at the dilution of 1:1600 was deposited on the slide and incubated overnight at 4°C. The WCs were repeated. Finally, the secondary antibody (Ab) solution (ThermoFisher Scientific anti-Rabbit I A32733), at the concentration of 0.5µg/mL, was incubated for 1h at 25°C and the WCs were repeated. Figure 25 depicts a schematic representation of the main steps in the immunoreaction protocols.

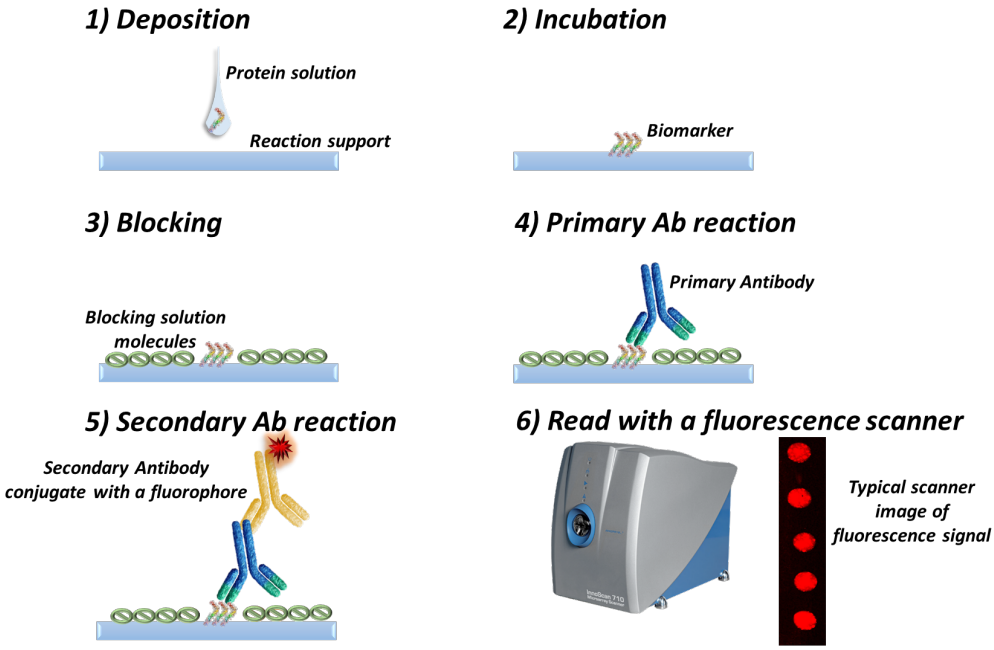

Figure 25. Schematic representation of the steps in the immunoreaction protocol.

3.6 Microarray scanner

A confocal fluorescence microarray scanner InnoScan 710 (Innopsys) was used for measuring the fluorescence signal (FS) emitted by the spots obtained on the target slide by the p-jet accumulation. The imaging system used the laser source at 635 nm for exciting the fluorescent molecules and two

digital photomultipliers (PMT) for recording the optical signal emitted by the molecules. Depending on the expected spot size and signal intensity, four main scan parameters can be adjusted: resolution (from 3 to 40 μm/pixel), speed (from 10 to 35 lines/s), gain PMT (linear from 0 to 100 %), laser power (5 and 10 mW). The TIFF 16-bit images captured by the scanner were evaluated quantitatively by Mapix software. Figure 26 shows a scanner image and a typical interface of the Mapix software.

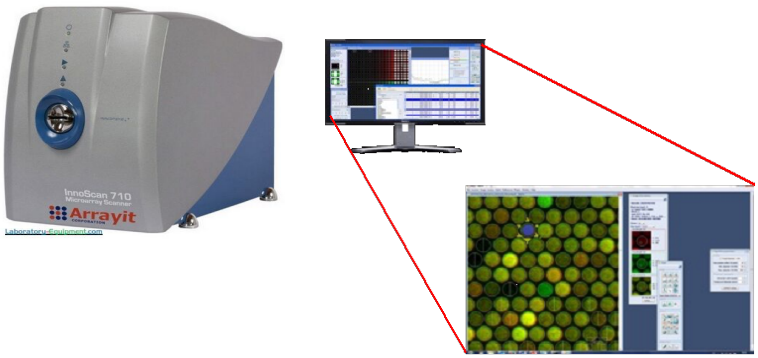

Figure 26. Picture of the Innoscan710 microarray scanner (left) and typical user interface of the Mapix software for spot acquisition and analysis.

3.7 The piezo-driven biospotter

The performance of the p-jet accumulation was compared to a commercial piezo-driven biospotter (S3 sciFLEXARRAYER, Scienion AG) using a set of fluorophore samples. S3 is a non-contact dispensing system designed to produce small sample spots from ultra-low volumes of biomaterials. Samples were dispensed on top of low auto-fluorescence glass microscope slides (Marienfeld, ref. 1010200) after a washing procedure, where the slides were first rinsed with acetone and isopropanol, and then dried with nitrogen blow (Topgun). Fluorophore samples were prepared by diluting Alexa Fluor 647 carboxylic acid tris(triethylammonium) salt (A33084 Invitrogen) in 12mM PBS (pH7,4) to achieve fluorophore concentrations for three ranges: (1) 0.01 pg/ml to 10 pg/ml, (2) 10 ng/ml to 1 μg/ml and (3) 3 μg/ml to 12.5 μg/ml. The dispensed individual drop size with S3 was 350-372 pl and distance between the nozzle and the sample slide was 282-500 μm. Three replicate sample slides were prepared for the three concentration ranges.

3.8 Drop dispensed schemes by biospotter

Three replicate sample slides were prepared for the three concentration ranges as shown in Figure 27. The number of dispensed drops per spot varied to produce different signal levels. An array of 2 x 4 spots was dispensed for each of these variations (concentration and drop amount), resulting in total amount of 24 spots for each concentration.

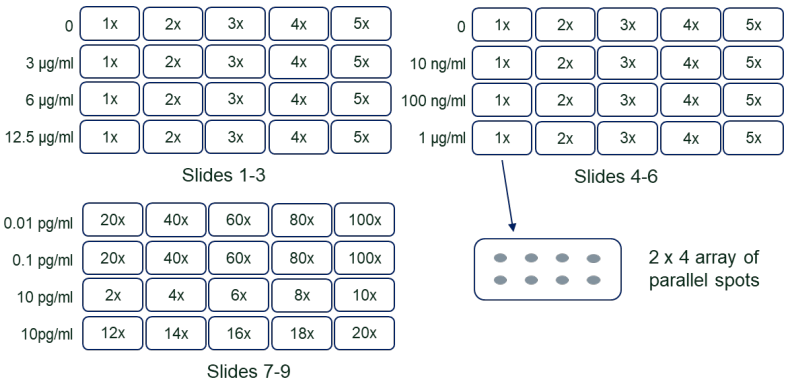

Figure 27. Number of dispensed drops per spot for each fluorophore concentration prepared for the comparative study by a commercial biospotter. Each variation of concentration and drop amount included 8 spots in a 2 x 4 array.

3.9 The pendant drop tensiometer

The surface tension (ST) measurements were performed in cooperation with the research group of Prof. Minale and Prof. Carotenuto, by using the pendant drop tensiometer (First Ten Angstroms FTA 1000, (see Figure 28a). Figure 28b shows a schematic representation of the instrument. The apparatus consists of a backlight source (25 mm blue LED) which is a specialized illumination positioned behind the drop sample. The image acquisition is realized with a digital camera equipped with a microscope objective (0.7X to 4.5X of magnification). The camera is connected to a computer for analyzing the data by using the software FTA 32 Video 2.1.

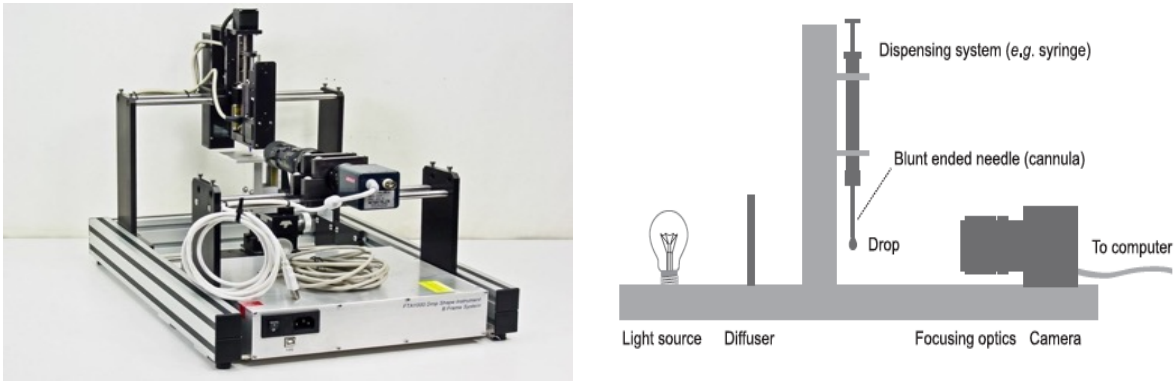

(a) (b)

Figure 28. (a) Picture of the pendant drop tensiometer First Ten Angstroms FTA 1000. (b) Schematic representation of the instrument.

The dispensing system is composed of a syringe with a volume of 250 µl to 26 nl and a needle from which is formed the drop, and an automated pump with a pumping velocity of 0.02 µl /s to 5 µl/s that controls the fluid release and the drop formation (see Figure 29).

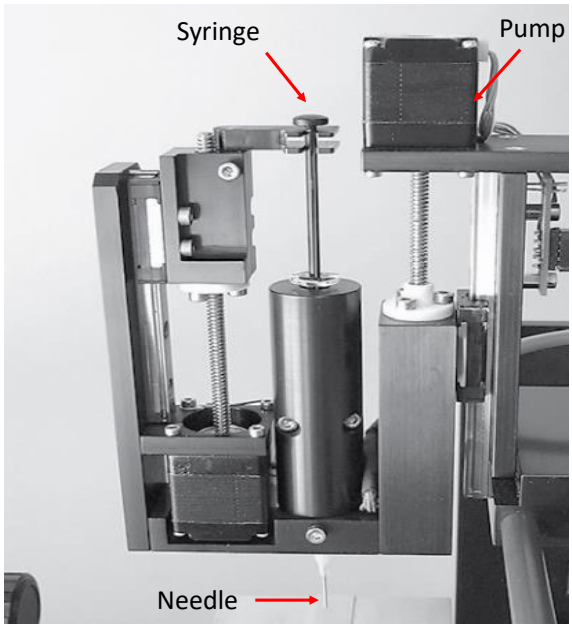

Figure 29. Picture of the dispensing system with main components indicated by the red arrows (needle; syringe; pump).

The measurement of the surface tension is based on the Drop Shape Method[59]. There are two principal assumptions, the drop is symmetric about a central vertical axis and the surface tension, and the gravity are the only forces shaping the drop. Surface tension is determined by fitting the shape of the drop (in a captured video image) with the Young-Laplace equation which relates interfacial tension to drop shape [60]. The shape of a drop is determined by its radii of curvature, R_1 and R_2. In the case of a spherical drop, these are equal. The radii are defined according to Adamson et al[61]. The relationship between interfacial pressure (the pressure across the interface) and these radii of curvature is called the Young-Laplace equation [62]:

$$\Delta P = \Delta \left(\frac{1}{R1} + \frac{1}{R2}\right) \quad (1)$$

Where ΔP is the interfacial pressure difference, γ is the interfacial tension, R_1, R_2 are surface's radii of curvature. In a column of fluid of density ρ and height h,

$$\Delta \mathrm{P} = \rho g h \quad (2)$$

and g is the acceleration due to gravity, (9.8m/s^2). The software does these steps automatically. Besides, to obtain the best results, the image must be in precise focus Figure 30 shows images of good size and focus.

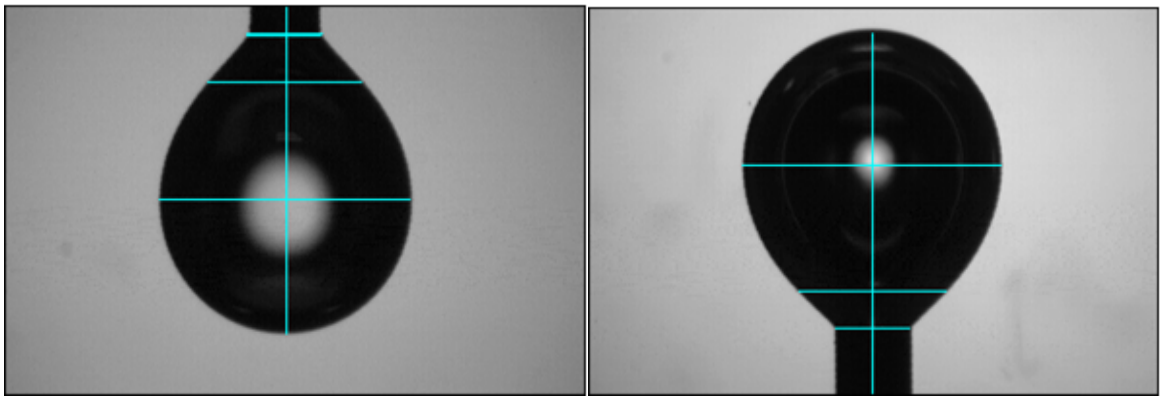

Figure 30. Typical image of the pendant drop recorded by the camera of the tensiometer.

3.10 Surface tension measurements

The STs (γ) of protein solutions were determined by using the tensiometer (First Ten Angstroms FTA 1000) equipped with software (FTA 32 Video 2.1). The instrument is described in section 3.9. The measurements were done at room temperature (24±1°C), in triplicate, and the drop profile was monitored up to a maximum time of 40 minutes. Besides, the measurements were repeated at different times during the protein storage, that was after the protein package opening. To this end, the investigation times were fresh protein solution (day 0), after one week (day 7), after two weeks (day 14), and after 1 month (day 30). Furthermore, all the tests were done on three different dilutions of the Aβ 1-42 protein solution (800 µg/mL, 400 µg/mL, and 40 µg/mL). The protocol for preparing these protein solutions was reported in the following section 3.11.

3.10.1 Defining the measurement protocol

Since it is important to preserve the droplet from environmental perturbances, the measurements were done in a homemade closed system (HCS) shown in Figure 31.

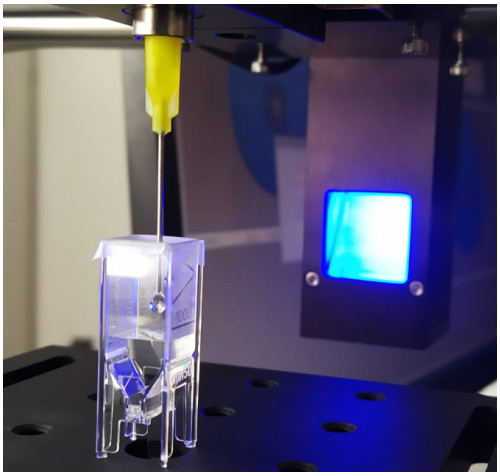

Figure 31. Picture of the cuvette used as homemade closed system for the surface tension measurements in a closed space.

The HCS was composed of a traditional plastic cuvette (Eppendorf® UVette®, Sigma-Aldrich) sealed by a Parafilm layer (Parafilm PM996, Sigma-Aldrich). The tip of the needle, with the pending droplet,

was in the sealed cuvette filled with 500 μL of distilled water. In this way the droplet environment was saturated and the evaporation rate attenuated significantly. The needle was inserted into the HCS simply by puncturing the Parafilm layer. The volume of the pendant drop (PndVol) was set at 15 μL, according to the requirements of the measurement system which needs drops with volumes ≥ 10μL[59]. A preliminary test campaign was performed to have a calibration of the HCS. The PndVols and the STs of distilled water were measured for 58 minutes with and without the HCS. Figure 32 shows the trends obtained.

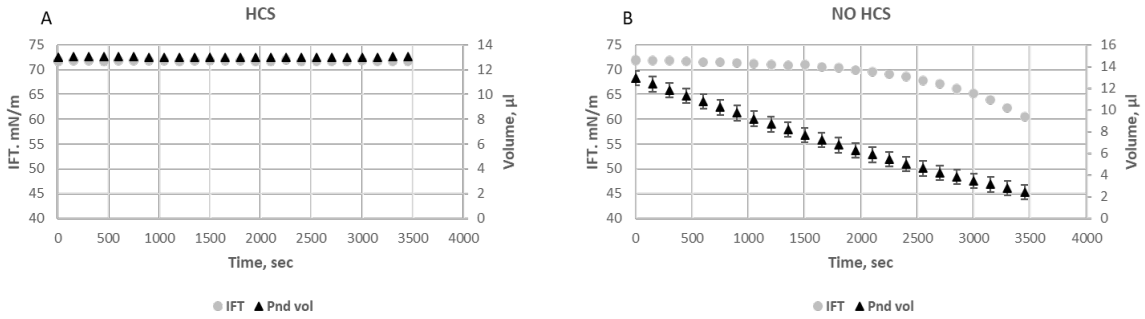

Figure 32. Trends of the ST and the volume obtained with and without the HCS.

The STs of distilled water were 72 mN/m±0.2 without the HCS and 71.8 mN/m±0.3 with the HCS. These values were coincident with the known value of the ST for distilled water (71.9 mN/m at 25°C)[63] with an acceptable error of 0.3% and 0.7% respectively. The ST with HCS was constant at value of 71.8 mN/m±0.3, whereas the ST without HCS had a variation of 16%. The PndVols recorded with the HCS remained constant at a value of 13μl±0.1. On the contrary, during the test without the use of the HCS, the PndVol was remarkably changed with a variation of 80%. As a result, the following STs measurements on the protein solutions were done by adopting the HCS.

3.10.2 Mathematical models

The phenomena which might be involved in the adsorption process of proteins at an air/water interface are proteins diffusion from the bulk towards the interface, adsorption/penetration at the interface, and unfolding and molecular rearrangement[64–70]. These steps are shown in Figure 33.

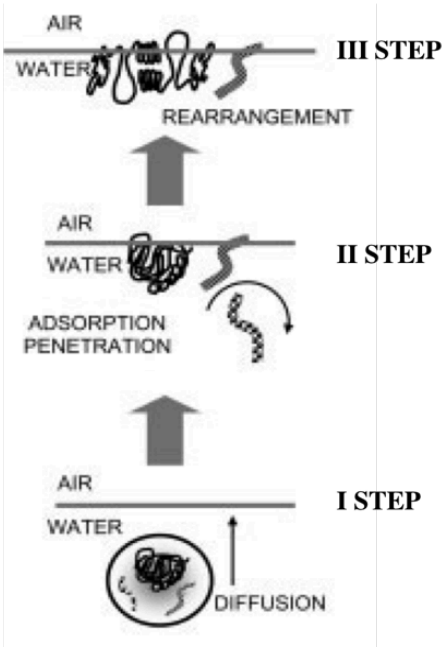

Figure 33. Steps involved in the adsorption processes of proteins at an air/water interface [71].

The first step related to the diffusion is described by the Ward-Torday equation[72]:

$$\pi = \gamma(t) - \gamma(0) = C_0 KT \frac{D_{diff} t}{\Pi} \quad (3)$$

Where π is the interfacial pressure at any time, $\gamma(t)$, $\gamma(0)$ are the surface tension at any time t and at time zero respectively, C_0 is the bulk concentration in the aqueous phase, K is the Boltzam constant, T is the absolute temperature, D_{diff} is the diffusion coefficient, Π is the Pi greco value[68]. By plotting the interfacial pressure π as a function of $t^{1/2}$ is possible to obtain the diffusion rate (k_{diff}) as the slope of the curvature[70]:

$$K_d = C_0 KT \left(\frac{D_{diff}}{\Pi}\right)^{1/2} \quad (4)$$

The second and the third steps are described with the Graham and Philips equation[73]:

$$ln\frac{(\pi_f - \pi_t)}{(\pi_f - \pi_0)} = -k_i t \quad (5)$$

where π_f, π_t, π_0 are the surface tension at the end of the adsorption processes, at any time and at t=0, respectively. The application of equation (5) can identify two linear regions with two different slopes, the initial slope is taken to correspond to a first-order rate constant of unfolding (K_{ads}), while the second slope is taken to correspond to a first-order rate constant of rearrangement (k_r)[64,66,68,70]. Besides, it is well known that the STs trends for proteins and surfactants may be characterized by an initial period where there was no change in the interfacial pressure (called *lag* or *induction*

period)[66,68,74]. This period is calculated by considering the change concavity of the curves obtained by applying the Ward-Torday equation. Figure 34 showed the definition of the lag time.

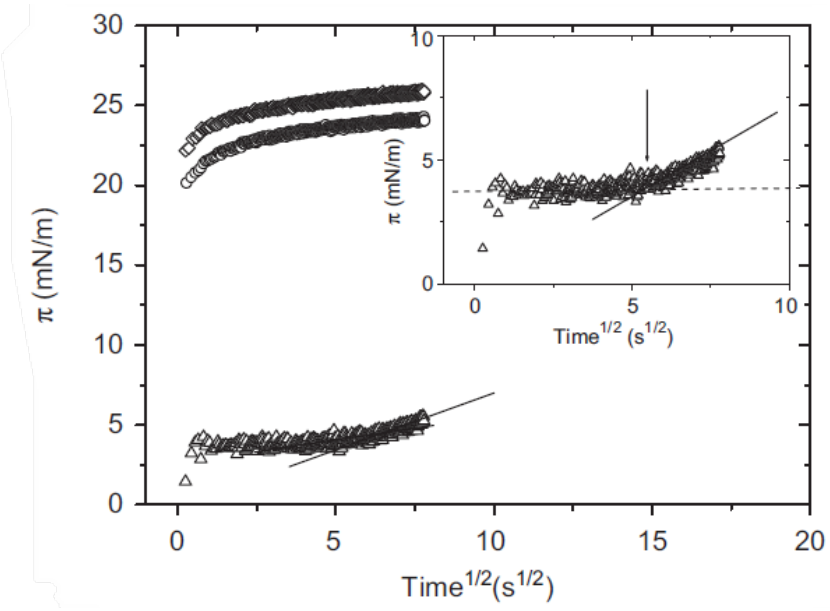

Figure 34. Definition of the lag period, which is indicated by an arrow[66].

3.11 Aβ 1-42 protein solutions

The surface tension measurements were carried out on the AD biomarker Aβ1-42 (Sigma Aldrich AG912). The white lyophilized powder was resuspended in 2mM of NaOH so that a stock solution was obtained (1mg/ml) as suggested by the datasheet and sonicated for 45 seconds. The serial dilutions were prepared with PBS1X (Gibco 10010023) to obtain four aliquots of each final concentration of 800 mg/mL, 400 mg/ml, and 40 mg/mL. The aliquots were stored at -20°C. On the day of use, the aliquots of interest were thawed. To ensure the same frozen-thawed process for all solutions measured, on day 0, the reconstitution day, an aliquot of 800 mg/mL, 400 mg/ml, and 40 mg/mL was frozen and thawed before the measurements.

3.12 Determination of the fluorescence intensity

Four droplets for each Aβ1-42 solution (800 µg/ml, 400 µg/ml, and 40 µg/ml) were deposited with a traditional pipette in the volume of 3 µl on the glass slide functionalized with 2D-Amine groups (Arrayit SuperAmine 2 Ultra Low Density, Cat. SMM2ULD). The immunoreaction protocol was reported in detail in Section 3.5. Afterward, the fluorescence intensity (FI) was evaluated by using the microarray scanner thoroughly described in Section 3.6. The scanner was set with the laser source at 635 nm for exciting the fluorescent molecules, the resolution was fixed at 10µm/pixel, the speed was 35 lines/s, the gain of the PMT was 5% and the laser power was 5mW. The TIFF 16-bit images captured by the scanner were evaluated quantitatively by Mapix software.

3.13 Statistical Analysis

The kinetic constants K_d, K_{ads}, and K_r of the concentrations 40μg/ml, 400 μg/ml, and 800μg/ml were determined on day 0, day 7, day 14, and day 30 by using the mathematical models described in section 3.10. To understand whether during the time the kinetic constants were subject to a significant change, statistical analyses were applied. The dependent variables were the kinetics constants, while the days were considered the qualitative variable. The first step was to assess the assumption of normality with the *Shapiro-Wilk test*, which verified the normal distribution of the data, obtaining in each case p-values>α(=0.05). Therefore, a parametric test the *One-Way ANOVA* was adopted. This test allowed us to compare the means of the kinetic constants evaluated on day 0, day 7, day 14, and day 30 and to verify if there were differences between day 0 and day 30. The Fisher's F test obtained reflected the probability corresponding to the F value, with Pr>F values that determined the significance of our results. Once ANOVA found the significant differences in our means, a post hoc test was selected, the *Dunn's Multiple Comparison test*. This test evaluated the groups with significant differences. The tests were performed with XLSTAT an add-on of Microsoft Office Excel (version Microsoft Office 365 Pro Plus).

Chapter 4 *Results and discussions*

4.1 Reproducibility of the p-jet spots

The p-jet technique was used for accumulating diluted biomolecules[43,48]. In the last years, the possibility of using the pyroelectric effect for accumulating micro-droplets and for detecting highly diluted biomolecules was demonstrated for the first time. Here, a completely new configuration was presented where a more compact and easier-to-use heating system was developed, compared to the CO_2 laser head or to the μ-heater used in our first papers mentioned above. This advanced experimental setup as well as the thermal stimulus for generating the pyroelectric effect were thoroughly described in Sections 2.3 and 2.5. The reproducibility of the spots generated by this new p-jet sensor was evaluated by printing around 100 replicates of spots obtained by delivering 1 to 5 droplets and 10 to 50 droplets at each position. The successive droplets are indicated here as jets, for brevity. The sample was the Alexa fluorescent probe (see Materials and Methods) at a concentration of 6 μg/mL. Soon after the delivery of one spot, the target slide by 1 mm with the precision translation stage was translated, then with successive spots was proceeded. Figure 35 shows a typical scanner image of the resulting spots, just as an example.

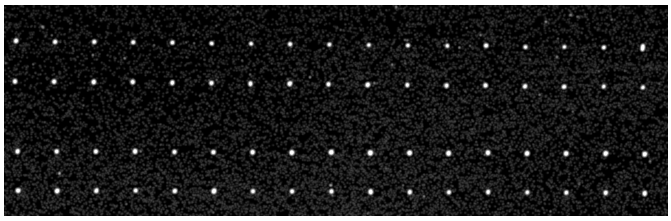

Figure 35. Scanner image of the typical p-jet spots obtained by spotting droplets of Alexa fluorescent probe.

The recorded scanner images were analysed by Mapix software. The diameter of the spots was on average 75 μm with a coefficient of variance of 5% for spots with 1-5 jets and 130 μm with a coefficient of variation of 7% for the spots with 10-50 jets. Therefore, the variation of spot diameter was negligible with the increasing number of jets in both ranges, and the FS data were analysed indifferently through 'F tot' or 'F mean' in the case of the p-jet spots. In fact, the first represents the sum of the gray values of all the pixels in the spot area and the second is F tot divided by the number of pixels in the spot area. In other words, the F mean values give information about the optical density of the spots. The FS had a variability of around 6% for the different groups of replicates at the same number of jets. These results demonstrate the significance of the data and the high repeatability of the p-jet spots in terms of both diameter and FS.

4.2 Characteristic curves of the p-jet accumulation

To test the reliability of this new p-jet configuration for tuning the accumulation rate of low abundant biomolecules, the behavior of the FS of the spots as a function of the number of droplets (referred to as jets) delivered for each spot was evaluated. It is well known that ELISA-based procedures represent the gold standard in most clinical diagnoses aimed to detect specific biomarkers in human fluids. Detection of Aβ1-42 in human cerebrospinal fluid for AD diagnosis is challenging for ELISA having LOD typically around 50 pg/mL, which prevents a reliable detection of these biomarkers in peripheral fluids such as blood, where the concentrations are expected to reach only sub-picogram levels. Considering the novelty of the technique, this study was performed first for three relatively high concentration values in the μg/mL range (12;6;3) and successively for three challenging concentrations less than the ELISA LOD mentioned above (10 pg/mL; 0.1 pg/mL; 0.01 pg/mL).

The pin with the Alexa probe sample at 12.5 μg/mL was loaded, and five spots were printed, the first with one jet and the others by accumulating two jets, three jets, four jets and five jets, respectively. Eight replicates for each spot were performed, and the same kind of experiment for the other two concentrations at 6 μg/mL and 3 μg/mL was repeated. Figure 36 shows the behavior of the FS as a function of the number of accumulated jets for the three concentrations at the μg/mL level.

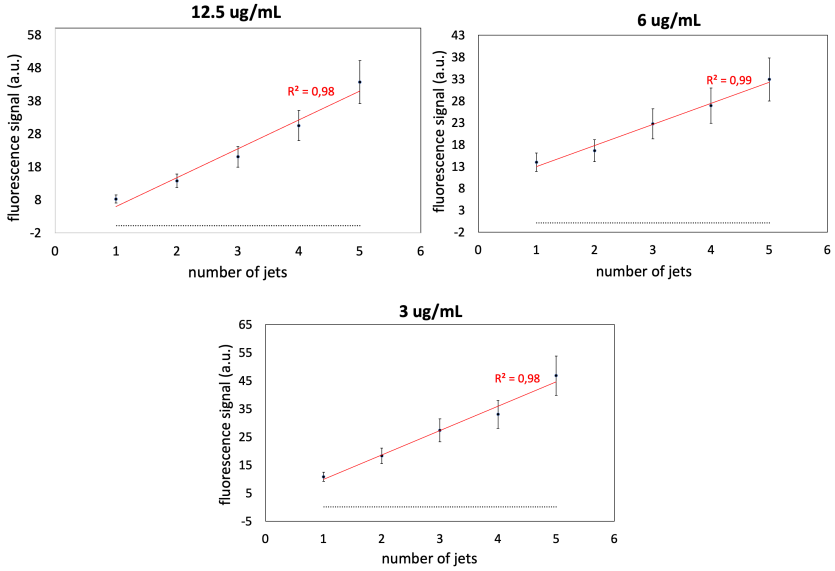

Figure 36. Fluorescence signal of the p-jet spots as a function of the increasing number of jets, for three concentrations of the Alexa probe. The signal values were averaged on eight replicates of the spots and the error bars correspond to their standard deviation. The linear plots were obtained by least squares fitting. The horizontal dashed lines correspond to the background level calculated as three times the standard deviation of the background FS.

The dashed lines correspond to the background level calculated as three times the standard deviation of the background signal. The data on the Y axis corresponds to the average FS over eight replicates of the spots calculated as mean gray values per unit area of the spots. These results show

that the optical density of the spots increased linearly with an increasing number of accumulated jets for each concentration, and the linear regression equations exhibited $R^2 \geq 0.98$.

After appropriate cleaning of the printing pin, the labelled antibody probe solution (see Materials and Methods) at the concentration of 10 pg/mL was loaded and ten spots with an increasing number of jets from one to ten were printed. On the same target slide, ten spots were deposited by simply touching the slide with the printing pin from one to ten times for each spot. We performed three replicates of the spots, and the fluorescence images of the slides by the scanner was recorded. The images were analyzed by Mapix and the resulting data were averaged over three replicates. **Fig.37(a)** shows the corresponding graph.

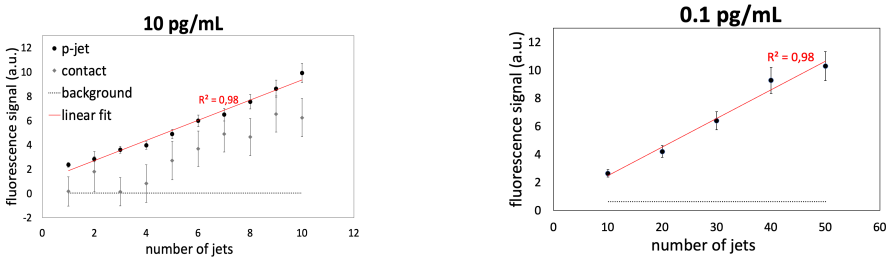

(a) (b)

Figure 37. Fluorescence signal of the p-jet spots for an increasing number of jets of the labelled antibody sample in case of (a) 10 pg/mL; (b) 0.1 pg/mL. In (a) we also report the results in case of 10 pg/mL by contact printing. Error bars represent their standard deviation resulting from three replicates of the spots. The linear plots were obtained by least-squares fitting. The horizontal dashed lines correspond to the background level calculated as three times the standard deviation of the background signal.

The results in **Fig.37(a)** demonstrate clearly that the contact-based accumulation does not behave linearly over the range of 1-10 touches, due to the cross-contamination occurring in successive touches of the pin on the same spot location. Moreover, the contact nature of this print method also means that during every deposition there is a chance that the pin tip may be damaged, thus worsening the repeatability in the deposited volume at each touch[75,76]. The lack of reliability was evident also through the behavior of the FS in the spots obtained with a few touches, where the signal is not detectable significantly over the background level. Conversely, the FS of the spots obtained by p-jet accumulation at 10 pg/mL is significantly higher than the background level, even for a few jets with an average signal/noise ratio (SNR) of 90 at one and two jets. Analogously to the case with the Alexa probe, also in this case the data show that the optical density of the spots increased linearly with the increasing number of accumulated jets, with linear regression equations exhibiting $R^2 \geq 0.99$.

The same kind of characterization was performed for 0.1 pg/mL to test the reliability of the p-jet accumulation at very challenging levels of concentration. Considering the two orders of

magnitude decrease in concentration the accumulation effect by using a higher number of jets, from 10 to 50 at a step of 10 was tested. Three replicates of the spots also in this case were performed and the fluorescence images of the slides by the scanner were recorded. The images were analyzed by Mapix and the resulting data were averaged over the three replicates (see **Fig.37(b)**). The SNR ranged from 6 to 14 and the spot optical density increased linearly in the whole range of jets. These results demonstrate the reliability of the p-jet in tuning linearly the rate of accumulation of biomolecules by the number of jets and in detecting fluorescence-labeled Ab2 proteins at challenging concentrations, thanks to the significant increase of the optical density.

4.3 Comparison with S3 biospotter dispensed samples

The performance of the new p-jet configuration was compared to a commercial piezo spotter S3 biospotter, in cooperation with the group of Sanna Uusitalo at the Technical Research Centre of Finland (VTT). S3 was used to dispense eight replicate sample spots with one to five dispensed jets at each position. The sample was the Alexa fluorescent probe (see Materials and Methods). The behavior was evaluated as a function of the number of jets for different concentration ranges. The first concentration range included 12.5ug/mL - 6ug/mL - 3ug/mL, the second 1ug/mL - 0.1ug/mL - 0.01ug/mL, the third 10pg/mL - 0.1pg/mL - 0.01pg/mL. The FS was measured by the scanner, and the images were analyzed by the Mapix software. Figure 38(a,b) shows the typical scanner images of the slides with spots at the second and third concentration ranges, respectively. Figure 38a shows that the spot diameter increased significantly with the number of jets, on average from 300 μm (1 jet) to 600 μm (5 jets), and Figure 38b shows the lack of significance of the spots at the challenging dilutions. The FS was analyzed here in terms of both F tot and F mean values and Figure 38(c-f) show the corresponding results.

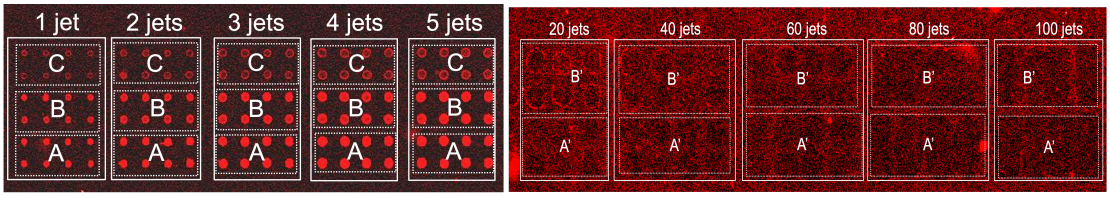

(a) **(b)**

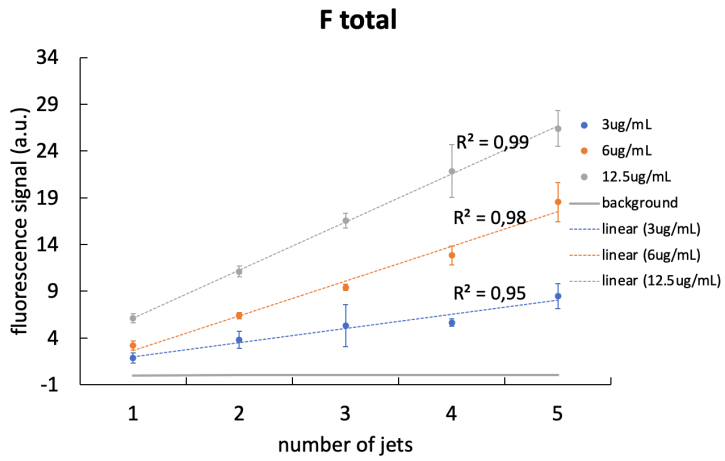
F total
fluorescence signal (a.u.)
number of jets
R² = 0,99
R² = 0,98
R² = 0,95
3ug/mL
6ug/mL
12.5ug/mL
background
linear (3ug/mL)
linear (6ug/mL)
linear (12.5ug/mL)

(c)

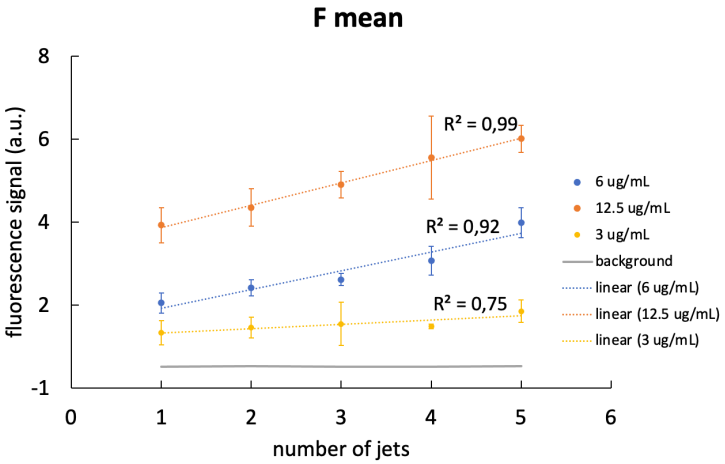
F mean
fluorescence signal (a.u.)
number of jets
R² = 0,99
R² = 0,92
R² = 0,75
6 ug/mL
12.5 ug/mL
3 ug/mL
background
linear (6 ug/mL)
linear (12.5 ug/mL)
linear (3 ug/mL)

(d)

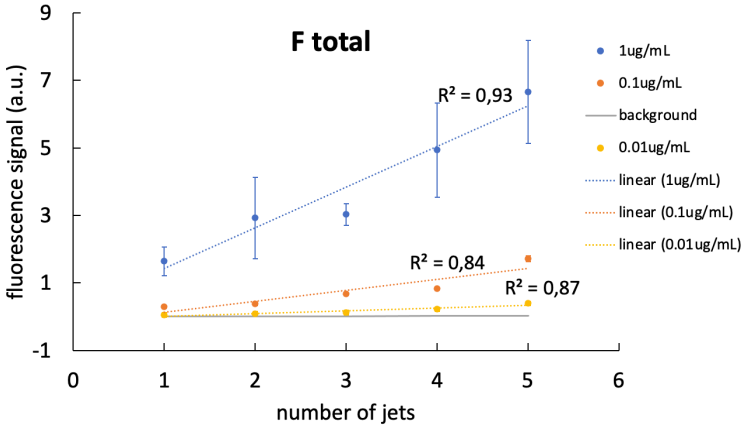
F total
fluorescence signal (a.u.)
number of jets
R² = 0,93
R² = 0,84
R² = 0,87
1ug/mL
0.1ug/mL
background
0.01ug/mL
linear (1ug/mL)
linear (0.1ug/mL)
linear (0.01ug/mL)

(e)

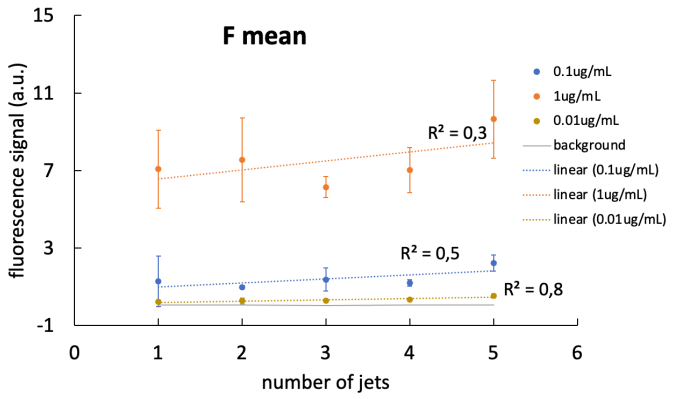

(f)

Figure 38. Biospotter results. (a,b) Typical scanner images of the slides with the spots at 1ug/mL (A), 0.1 ug/mL (B), 0.01ug/mL (C), 0.1pg/mL (A') and 0.01pg/mL (B'); (c,e) F tot as a function of the number of jets for the concentrations in the ranges 12.5ug/mL-3ug/mL and 1ug/mL-0.01ug/mL, respectively; (d,f) F mean as a function of the number of jets for the concentrations in the ranges 12.5ug/mL-3ug/mL and 1ug/mL-0.01ug/mL, respectively. The data in (c-f) were averaged over eight replicates of the spots with error bars corresponding to their standard deviation. The linear functions were obtained by weighted least-square method. The average diameter in (a) is 300 μm for 1 jet and 600 μm for 5 jets.

Both F tot and F mean increase with the number of jets for all the concentration ranges. However, while F tot increases on average by a factor of five and six in the first and second concentration range respectively (see Figure 38(c,e)), the F mean increases only by a factor of two in all samples (see Figure 38(d,f)). This means that the increase in spot optical density is negligible for increasing jets, thus preventing the accumulation effect achieved instead by p-jet. In fact, the spots at challenging concentrations have SNR < 1, even up to 100 jets (see Figure 38b). Moreover, linear regressions with $R^2 \geq 0.98$ were achieved only for the F tot values at 12.5 μg/mL and 6 μg/mL and for F mean values at 12.5 μg/mL, thus demonstrating the lack of linear behavior for all the concentrations below the μg/mL level. These results demonstrated that the accumulation rate achievable through the p-jet sensor is unique and not reachable through a commercial piezo-driven dispensing biospotter, thus launching the p-jet as a new tool for sub-picogram detection of biomolecules.

4.4 Application for immunodetection of Aβ1-42

The p-jet technique was tested for a real application of immune-detection by using the biomarker Aβ1-42. It belongs to the family of biomarkers object of clinicians' interest in the diagnosis of AD. This study had attention to a set of concentration values falling in the challenging range of pg/mL. Three spots were produced with 20 accumulated droplets for each concentration value. The spot images were recorded by the scanner and evaluated by Mapix. Figure 39 shows the resulting data averaged over three replicates of the spots.

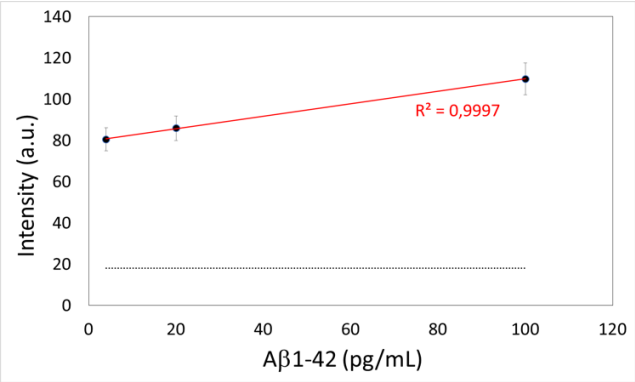

Figure 39. Mean fluorescence intensity of the p-jet spots of Aβ1-42 with increasing solution concentration. Error bars represent the standard deviation of three replicated spots. The linear plot was obtained by least-square fitting. The horizontal dashed line corresponds to the background level calculated as three times the standard deviation of the background signal.

These results demonstrate the reliability of the p-jet for detecting Aβ1-42 onto a solid surface through an immunoreaction protocol, with a linear behaviour in the pg/mL range of concentrations, below the current limits of traditional ELISA kits. In perspective, this technique would simplify the detection of low abundant biomolecules by accumulating them directly onto the reaction slide and by using sub-microliter volumes of reaction, with significant advantages in all those cases where diagnostic applications must be performed with very small volumes of the analyte. A new p-jet sensor with the ability to enhance the fluorescence signal of low abundant biomolecules linearly by increasing the number of accumulated jets. This technique provides an easy-to-use procedure that can tune the accumulation rate of target molecules in highly diluted solutions. The reliability of the technique has been demonstrated for a fluorescent probe with a concentration falling well below the current limit of detection using standard ELISA methods, down to a sub-picogram level. Moreover, the technique has been demonstrated to be reliable also for a typical case of clinical interest, namely for detecting biomarkers of AD through an immunoreaction protocol, with a linear behavior in the pg/mL range. In perspective, this p-jet technique can be exploited in a wide range of clinical cases where the clinician needs to determine the amount of low abundant biomarker molecules in peripheral human fluids to perform an early diagnosis, as in the case of AD biomarkers.

4.5 Surface tension measurements

The STs (γ) of the protein solutions (800 µg/ml, 400 µg/ml, and 40 µg/ml) were evaluated as described in Section 3.9. Figure 39 shows that Aβ1-42 solutions 800 µg/ml and 400 µg/ml (day 0), had the typical sigmoidal trends common for proteins and emulsifiers[70]. Specifically, two different regions, corresponding to unsaturated and saturated adsorption layers (plateau regions), were observed (see Figure 40). In fact, when an aqueous solution is in contact with an air phase, a finite

time is required for the surface-active species to diffuse, adsorb at the interface, and reach the equilibrium value[77]. The equilibrium values (γ_{eq}) were determined from the plateau regions and were equal to 43±0.6 mNm^{-1} for 800 μg/mL and 44±0.8 mNm^{-1} for 400 μg/mL. Whereas the initial surface tension (γ_0) values were 55±1mNm^{-1} for 800μg/mL and 61±0.4 mNm^{-1} for 400 μg/mL. In the case of Aβ1-42 at the concentration of 40 μg/ml, during the first 3 minutes, no surface tension decrease was observed, but the ST remained constant at a value of 71.3±0.2 mNm^{-1}. Besides, it took more than 40 minutes for equilibrium to be attained (see Figure 39). On the contrary, for higher concentrations (800 μg/mL, 400 μg/mL) the STs quickly decreased as observed for usual surfactants and proteins[78], and the equilibrium was reached in 20 minutes. The ST for the control solution (0 μg/mL) was 71±0.2 mNm^{-1} and remained constant at this value for the 40 minutes considered, highlighting that the Aβ1-42 was a surface-active species and, this determined the ST decrease. These first considerations were thoroughly investigated by using the mathematical models described in section 3.10.2, and by obtaining the graph reported in Figure 41.

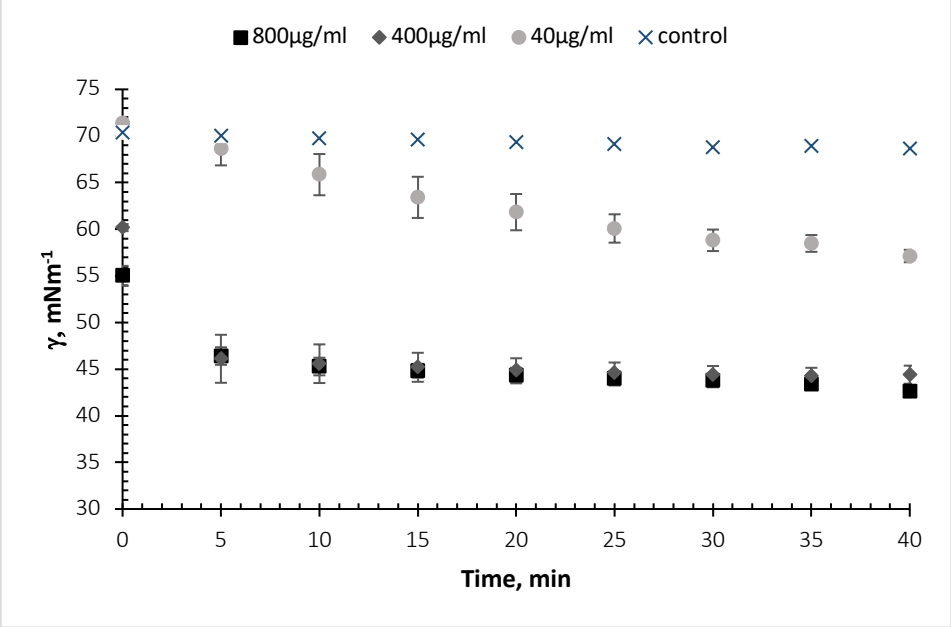

Figure 40. STs trends of Aβ1-42 solutions at 800 μg/mL (black square), 400 μg/mL (grey diamond), 40 μg/mL (light grey circle), 0 μg/mL (blue x).

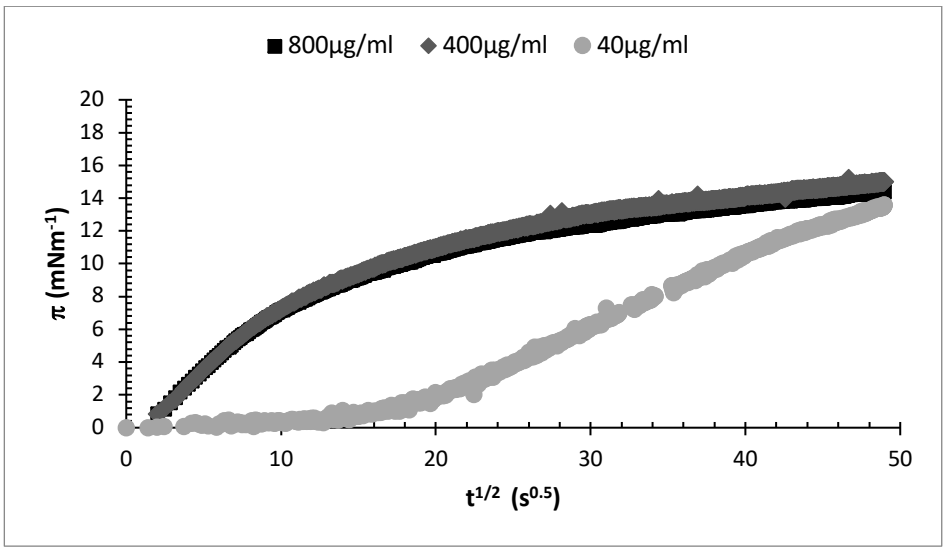

Figure 41. Temporal evolution of surface pressure, π, of Aβ1-42 at the air/water interface, at 800 μg/mL (black square), 400 μg/mL (grey diamond), 40 μg/mL (light grey circle). Data are reported as a function of time, t, square root according to Eq. (3). Error bars are not reported to make the figure more readable. The standard error was computed over three repetitions and is lower than 10%.

Data arranged according to equation (3) were reported in Figure 41, they have shown that at day 0, the lowest concentration (40 μg/ml) was characterized by an initial period where there was no change in the interfacial pressure (*lag* or *induction* period)[68,74]. Conversely, for the highest concentrations, the interfacial pressure immediately changed. These results agreed with the literature data for proteins, it is well-known that the induction period shortens as protein concentration is increased[79,80]. In fact, for the highest concentrations, no lag period was observed but the induction time was found to decrease as the bulk concentration was increased. The induction is caused by two factors: first, proteins may have a critical surface concentration only above which they can engage in intermolecular cohesive interactions at the interface and cause a greater reduction in surface tension. Second, it might be related to the time needed for the adsorbed proteins to unfold at the interface and to initiate cohesive interactions[78–84]. In this second case, the induction period is dependent on the protein stability[85]. Since the 40 μg/mL was quite diluted, the induction period (143 seconds, as reported in Table 8) at day 0 could be related to the insufficient adsorption of Aβ1-42 to the interface. In other words, the number of adsorbed proteins was not enough, thus, the interactions between them were not appreciable and the ST did not change. Even though on day 0 for the higher concentrations (800 and 400 μg/mL), there was no induction period (see Figure 41), it was noteworthy to notice that on day 30, the lag period arose for the concentration of 400 μg/mL and it increased for the 40 μg/mL (see Figure 42b and Table 8). This was an outstanding result, suggesting that the protein stability was changing over time.

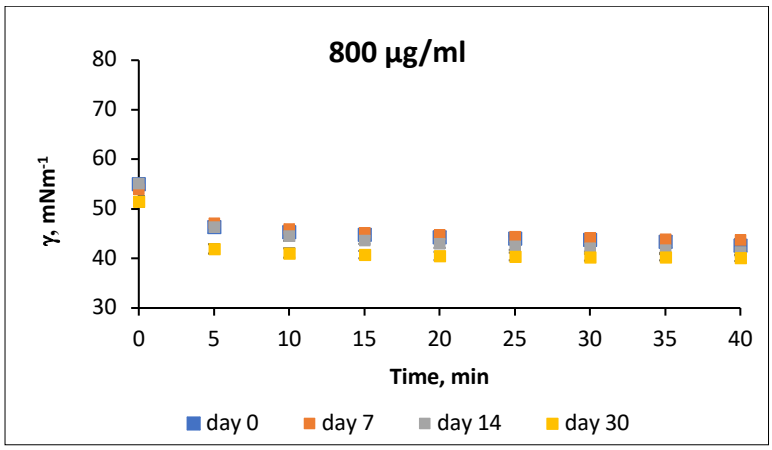

(a)

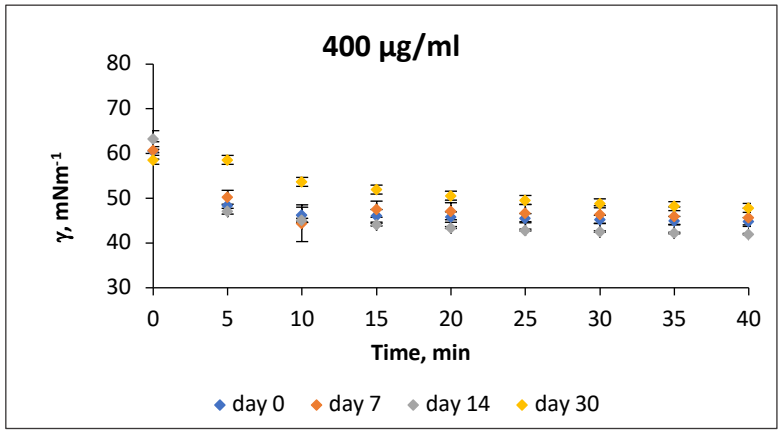

(b)

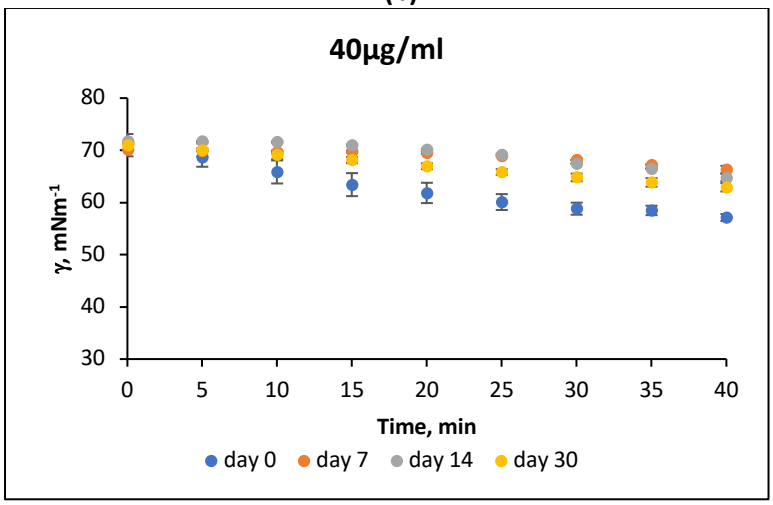

(c)

Figure 42. STs trends of Aβ1-42 (a) 800 µg/ml at day 0 (blue square), day 7 (orange square), day 14 (grey square), day 30 (yellow square), (b) 400 µg/ml at day 0 (blue diamond), day 7 (orange diamond), day 14 (grey diamond), day 30 (yellow diamond), (c) 40 µg/ml at day 0 (blue circle), day 7 (orange circle), day 14 (grey circle), day 30 (yellow circle).

Additionally, the kinetic constants (K_d, K_{ads}, and K_r) and the lag times were extrapolated as described in section 3.10.2 and were summarized in Table 8. From day 0 to day 30, in the case of 800 µg/ml, the results of the ANOVA test (Pr>F=8%) suggested that K_d did not significantly vary as well as the K_{ads}. This evidence can be attributed to the fact that 800 µg/ml was a concentration very high, so,

the solution was extremely crowded in proteins, and these were so close to each other to constrain their diffusion and adsorption at the interface. As a result, the processes (diffusion, adsorption) were extremely slow, and the corresponding kinetics did not remarkably change over time**.** Conversely, for the lower concentration (40 μg/ml), the K_d decreased significantly over time (Pr>F=0.3%). Moreover, the Dunn test highlighted that there was a significant difference in the K_d between day 0 and day 30 (Pr>Diff=0.001). The same result was obtained in the case of 400 μg/ml, the K_d remarkably decreased from day 0 to day 30 (Pr>Diff=0.001).

These results suggested that the protein on day 30 was diffusing slower than on day 0, probably due to its agglomeration. In fact, as the number of proteins as single entities in the volume solution decreased, the number of agglomerates increased, and these agglomerates diffused slower. In fact, the agglomerates were bigger than the single proteins and their diffusion was hindered. Besides, for 40 μg/ml the K_{ads} did not change over time (Pr>F=6%). The solution of 40 μg/ml was too diluted; thus, the adsorbed proteins were not so many to see variations in terms of adsorption during the time. Whereas, in case of 400 μg/ml the proteins adsorbed at the interface were sufficient to verify that K_{ads} changed over time (Pr>F=0.01%). Specifically, there was a decrease between day 0 and day 30 (Pr>Diff=0.01%). Since there were fewer proteins that could diffuse due to the presence of agglomerates, clearly, fewer of them were adsorbed at the interface, so K_{ads} decreased. Even though the proteins adsorbed at the interface in the case of 40 μg/ml were not sufficient to evaluate a K_{ads} variation over time, Table 8 shows that K_{ads} for the 40 μg/ml was higher than K_{ads} for the 400 and 800 μg/ml. This result was attributed to the adsorption process at the interface. In fact, proteins for adsorbing at the interface must expose their hydrophobic part to the interface and their hydrophilic part to the bulk, this structural disposition needs time. This time decreases as the protein concentration decreases. In fact, proteins in diluted conditions can easier move and find the right disposition at the interface, thus they are faster adsorbed. On the contrary, when the concentration was higher the interface was protein crowded and it was hard to move and find the right position, hence, to adsorb at the interface.

	40μg/ml				**400μg/ml**				**800μg/ml**			
	t_{lag} s	K_d $mNm^{-1}s^{-0.5}$	K_{ads} 10^{-3}, s^{-1}	K_r 10^{-3}, s^{-1}	t_{lag} s	K_d $mNm^{-1}s^{-0.5}$	K_{ads} 10^{-3}, s^{-1}	K_r 10^{-3}, s^{-1}	t_{lag} s	K_d $mNm^{-1}s^{-0.5}$	K_{ads} 10^{-3}, s^{-1}	K_r 10^{-3}, s^{-1}
day 0	143	0.4	3	/	/	1.5	1.3	3.5	/	0.8	1.1	/
day 7	498	0.1	5	/	/	0.8	1.2	2.9	/	0.5	1.2	/
day 14	400	0.1	0.7	/	2	1.4	1.5	4.0	/	0.6	1.3	/
day 30	400	0.1	0.6	/	3.82	0.4	0.5	1.0	/	0.7	1.5	/

Table 8. Velocity of diffusion (K_d), adsorption (K_{ads}) and rearrangement (K_r) for Aβ1-42 solutions at 40 μg/ml, 400 μg/ml and 800 μg/ml, evaluated at day 0, day 7, day 14 and day 40.

Concerning the rearrangement step, for 800 μg/ml was not found (see Table 8) since the proteins were so many and so crowded that they cannot do any movement/rearrangement at the interface.

For 40 µg/ml the solution was too diluted that more time would have been needed to see the rearrangement. On the other hand, in the case of 400 µg/ml was possible to evaluate a rearrangement step (see Table 8). Since the Critical Micellar Concentration (CMC) was reached at 400 µg/ml (see Figure 43), this was the optimal condition to have protein movement on the interface.

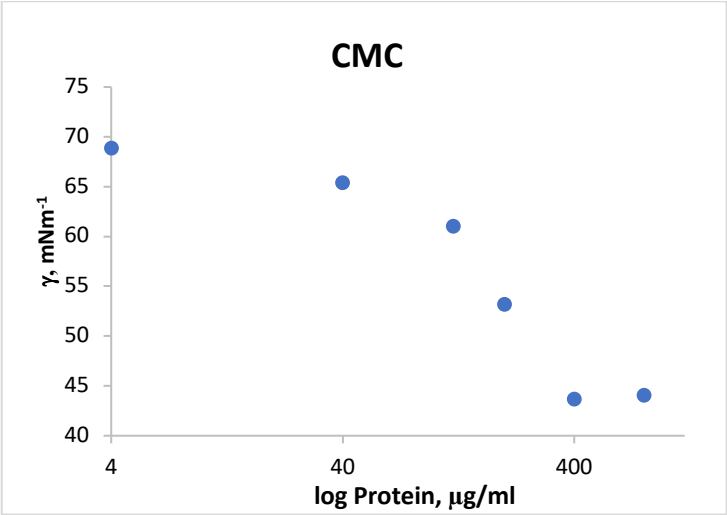

Figure 43. CMC evaluation, the concentration tested were: (0.4, 4, 40, 120, 200, 400, 800)µg/ml.

4.6 Fluorescence intensity measurements

To verify the hypothesis about the influence of protein agglomeration on the sensitivity of an AD diagnostic test, an immunoreaction protocol was carried out, so the FIs were evaluated. The results showed that at day 0 the FIs were equal to (6.21 ± 0.64)E+07 a.u. for 800 µg/ml and 400 µg/ml and to (3.59 ± 0.68)E+07 a.u. for 40 µg/ml. In the case of 40 µg/ml, there was no significant difference between groups (Pr>F=6%). This result could be explained considering that the immunoreaction protocol was realized by depositing the protein with a traditional pipette, this method was constrained by the diffusion effects of the molecules on the reaction slide, which drastically reduced the LOD. For instance, the lack of manual deposition of biomolecules was thoroughly described in our previous papers[41–43,48]. As a result, for the lower concentration, the sensitivity was not sufficient to detect a change in terms of FI. Whereas for 400µg/ml and 800 µg/ml significant differences (Pr>F=0.01%) were found over time. Specifically, it was proved that the FI on day 30 was significantly different from the FI on day 0 (Pr>Diff=0.01%). In fact, as shown in Figure 44 the FIs drastically decreased on day 30, for 800µg/ml and 400µg/ml.

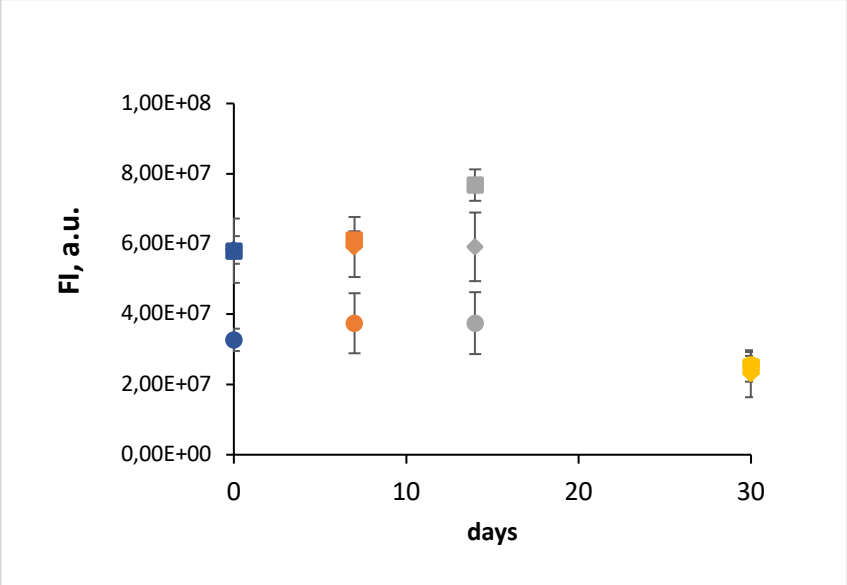

Figure 44. FIs trends of Aβ1-42 at concentration of 800 µg/ml at day 0 (blue square), day 7 (orange square), day 14 (grey square), day 30 (yellow square), of 400 µg/ml at day 0 (blue diamond), day 7 (orange diamond), day 14 (grey diamond), day 30 (yellow diamond), of 40 µg/ml at day 0 (blue circle), day 7 (orange circle), day 14 (grey circle), day 30 (yellow circle).

Chapter 5 *General conclusions and future perspectives*

The innovative pyro-electrodynamic jet (p-jet) method has been used as a printing device for viscous fluids and for applications in the field of high sensitive biosensors. In this Ph.D. thesis, the focus was on the p-jet method used for detecting biomolecules at the sub-picogram level. In this scenario, a p-jet configuration was proposed as a novel technique that could be implemented in future in a diagnostic tool for early diagnosis applications. The p-jet is based on the hydro-electrodynamic effect on the fluid, generated by an electric field activated pyroelectrically by a lithium niobate crystal. The operating principle is extremely simple and effective. A mother drop containing the biomolecules to be detected is split into many small droplets and stacked in a limited area of the deposition slide, in this way, the diffusion phenomena that limit the detection of low abundant molecules were eliminated, and therefore sensitivity was increased. Furthermore, this innovative p-jet sensor was extremely versatile since it can also be used to identify biomarkers present in very low concentrations in the blood related to pathologies such as Alzheimer's disease. It is easy to predict the social impact of this advanced technology, since, as in the case of AD disease, which has a high incidence and is currently without a cure, its early diagnosis would lead to an advanced study of the disease in the early stages of human beings and therefore the identification of possible treatments. Furthermore, the p-jet technique would open the route to a high sensitive biosensor significantly useful for non-invasive diagnosis procedures. Hospitalization and withdrawal of the patient’s spinal fluid with very delicate procedures that require specialized and qualified personnel would be no more necessary. This technology will enable faster and non-invasive early diagnosis of diseases in the future simply through routine blood tests, thus paving the way for highly efficient screening programs among the population.

In summary, this multipurpose technology opens the way to all those applications where the manipulation of small volumes of fluids is necessary and the need to detect low abundant molecules with important repercussions in the diagnostic field. Specifically, in the first part of this Ph.D. thesis, this new p-jet sensor with the ability to enhance the fluorescence signal of low abundant biomolecules linearly by increasing the number of accumulated jets was presented. This technique provides an easy-to-use procedure that can tune the accumulation rate of target molecules in highly diluted solutions. The reliability of the technique has been demonstrated for a fluorescent probe with a concentration falling well below the current limit of detection using standard ELISA methods, down to a sub-picogram level. In fact, the p-jet sensor was proven to have a limit of detection down to sub-picogram level, with a velocity in dispensing droplets of 1 drop/sec. Moreover, this sensor provides highly reproducible spots with a coefficient of variation below 10% both in diameter and intensity. The technique has been demonstrated to be reliable for a typical case of clinical interest, namely for detecting biomarkers of AD through an immunoreaction protocol, with a linear behavior in the pg/mL range. In perspective, this p-jet technique can be exploited in a wide range of clinical

cases where the clinician needs to determine the amount of low abundant biomarker molecules in peripheral human fluids to perform an early diagnosis, as in the case of AD biomarkers. The results achieved so far were promising, we believe that the p-jet sensor can be used also in the case of bodily fluids like urine and saliva. Concerning this aspect, preliminary results have been already collected.

Additionally, another important aspect to consider in studying AD is the conformational stability, such as the agglomeration of the biomarkers involved in the disease diagnosis techniques. The investigation of protein agglomeration was extremely important and was carried out in cooperation with the research group of Prof. Minale and Prof. Carotenuto. On the one hand, understanding protein agglomeration may predict the progress of AD, on the other, this phenomenon can compromise the sensitivity of the diagnostic test for AD disease. Therefore, in the second part of this Ph.D. thesis, a simple method to investigate protein agglomeration was presented. This innovative method was characterized by surface tension measurements of Aβ1-42 solutions and by the application of mathematical models for extrapolating kinetic parameters to evaluate the protein structure modifications. Moreover, to verify the hypothesis about the influence of the protein agglomeration on the sensitivity of an immunoreaction test, the surface tension measurements were coupled to an immunoreaction protocol for demonstrating that the fluorescence signal could decay as the protein agglomerates over time. As a result, we were successful in defining a method to evaluate protein agglomeration non-destructive and very easy compared to the traditional ones[26,27]. Results showed that for 800 μg/ml the agglomeration was not observed, whereas for 400 μg/ml and 40 μg/ml an agglomeration effect over time on the protein conformational stability was verified. Besides, by using the immunoreaction protocol a decay of the FI was identified in the case of 800 and 400 μg/ml, while it was not possible to find a significant decay of the FI for 40 μg/ml. This result was due to the lack of sensitivity of the method in the case of diluted solutions. All things considered, for 400 μg/ml the effect of protein agglomeration on an AD immunoreaction test was proved. Firstly, the protein agglomeration was verified (K_d decreased, induction time increased), then the FI was evaluated and showed that it drastically decreased as the protein agglomerated over time. However, the results have also demonstrated that the method proposed for defining the protein agglomeration was strictly dependent on the solution concentration. In fact, it was verified that for finding the aggregation effects a concentration too high, as 800 μg/ml, was not recommended. This result could be caused by the fact that for 800 μg/ml, the solution was extremely crowded in proteins, and these were so close to each other to constrain their diffusion and adsorption at the interface. As a result, the processes (diffusion, adsorption) were extremely slow, and the corresponding kinetics did not remarkably change over time**.** Conversely, it was possible to evaluate the protein aggregation in the case of 400 μg/ml and 40 μg/ml. We believe that by adopting this method for pathological samples

of AD-affected patients and by investigating the protein agglomeration the progress of AD could be evaluated.

References

1. Blennow, K., Hampel, H., Weiner, M. & Zetterberg, H. Cerebrospinal fluid and plasma biomarkers in Alzheimer disease. *Nature Reviews Neurology* vol. 6 131–144 Preprint at https://doi.org/10.1038/nrneurol.2010.4 (2010).

2. Urraca, J. L. *et al.* Polymeric complements to the Alzheimer's disease biomarker β-amyloid isoforms Aβ1-40 and aβ1-42 for blood serum analysis under denaturing conditions. *J Am Chem Soc* **133**, 9220–9223 (2011).

3. Ngoepe, M. *et al.* Integration of biosensors and drug delivery technologies for early detection and chronic management of illness. *Sensors (Switzerland)* vol. 13 7680–7713 Preprint at https://doi.org/10.3390/s130607680 (2013).

4. Wang, J. Electrochemical glucose biosensors. *Chemical Reviews* vol. 108 814–825 Preprint at https://doi.org/10.1021/cr068123a (2008).

5. Li, C. *et al.* Improvement of enzyme-linked immunosorbent assay for the multicolor detection of biomarkers. *Chem Sci* **7**, 3011–3016 (2016).

6. Gil Rosa, B. *et al.* Multiplexed immunosensors for point-of-care diagnostic applications. *Biosens Bioelectron* **203**, (2022).

7. Chen, Y., Liu, J., Yang, Z., Wilkinson, J. S. & Zhou, X. Optical biosensors based on refractometric sensing schemes: A review. *Biosens Bioelectron* **144**, 111693 (2019).

8. Wang, W., Chen, C., Qian, M. & Zhao, X. S. Aptamer biosensor for protein detection using gold nanoparticles. *Anal Biochem* **373**, 213–219 (2008).

9. Galozzi, S., Marcus, K. & Barkovits, K. Amyloid-β as a biomarker for Alzheimer's disease: quantification methods in body fluids. *Expert Rev Proteomics* **12**, 343–354 (2015).

10. Peña-Bautista, C. *et al.* Plasma lipid peroxidation biomarkers for early and non-invasive Alzheimer Disease detection. *Free Radic Biol Med* **124**, 388–394 (2018).

11. Pawlik, P. & Błochowiak, K. The role of salivary biomarkers in the early diagnosis of Alzheimer's disease and Parkinson's disease. *Diagnostics* vol. 11 Preprint at https://doi.org/10.3390/diagnostics11020371 (2021).

12. Morales-Narváez, E., Montón, H., Fomicheva, A. & Merkoçi, A. Signal enhancement in antibody microarrays using quantum dots nanocrystals: Application to potential Alzheimer's disease biomarker screening. *Anal Chem* **84**, 6821–6827 (2012).

13. Vestergaard, delanji, Kerman, K. & Tamiya, E. An Overview of Label-free Electrochemical Protein Sensors. *Sensors* **7**, 3442–3458 (2007).

14. Piriya V.S, A. *et al.* Colorimetric sensors for rapid detection of various analytes. *Materials Science and Engineering C* vol. 78 1231–1245 Preprint at https://doi.org/10.1016/j.msec.2017.05.018 (2017).

15. Kitamura, Y. *et al.* Plasma protein profiling for potential biomarkers in the early diagnosis of Alzheimer's disease. *Neurol Res* **39**, 231–238 (2017).

16. Nakamura, A. *et al.* High performance plasma amyloid-β biomarkers for Alzheimer's disease. *Nature* **554**, 249–254 (2018).

17. Janelidze, S. *et al.* Plasma β-amyloid in Alzheimer's disease and vascular disease. *Sci Rep* **6**, (2016).

18. Khoonsari, P. E. *et al.* Improved differential diagnosis of Alzheimer's disease by integrating elisa and mass spectrometry-based cerebrospinal fluid biomarkers. *Journal of Alzheimer's Disease* **67**, 639–651 (2019).

19. de Plano, L. M. *et al.* Innovative IgG Biomarkers Based on Phage Display Microbial Amyloid Mimotope for State and Stage Diagnosis in Alzheimer's Disease. *ACS Chem Neurosci* **11**, 1013–1026 (2020).

20. 359325a0.

21. Selkoe, D. J. *Alzheimer's Disease: Genes, Proteins, and Therapy*. http://physrev.physiology.org (2001).

22. de Genst, E., Messer, A. & Dobson, C. M. Antibodies and protein misfolding: From structural research tools to therapeutic strategies. *Biochimica et Biophysica Acta - Proteins and Proteomics* vol. 1844 1907–1919 Preprint at https://doi.org/10.1016/j.bbapap.2014.08.016 (2014).

23. Ann, M., Coon, D. W., Davies, H., Mckibben, C. & Gallagher-Thompson13, D. *The Psychological Impact of Genetic Testing for Alzheimer Disease*. *GENETIC TESTING* vol. 3 (1999).

24. Koedam, E. L. G. E. *et al.* Early-onset dementia is associated with higher mortality. *Dement Geriatr Cogn Disord* **26**, 147–152 (2008).

25. Mendez, M. F. Early-onset Alzheimer disease and its variants. *CONTINUUM Lifelong Learning in Neurology* vol. 25 34–51 Preprint at https://doi.org/10.1212/CON.0000000000000687 (2019).

26. Pedersen, J. T. & Heegaard, N. H. H. Analysis of protein aggregation in neurodegenerative disease. *Anal Chem* **85**, 4215–4227 (2013).

27. Mahler, H. C., Friess, W., Grauschopf, U. & Kiese, S. Protein aggregation: Pathways, induction factors and analysis. *Journal of Pharmaceutical Sciences* vol. 98 2909–2934 Preprint at https://doi.org/10.1002/jps.21566 (2009).

28. Nalwa, H. S. *Handbook of advanced electronic and photonic materials and devices*. (Academic, 2000).

29. Pyroelectricity: From Ancient Curiosity to Modern Imaging Tool.

30. Damjanovic, D. *Ferroelectric, dielectric and piezoelectric properties of ferroelectric thin films and ceramics*. *Rep. Prog. Phys* vol. 61 (1998).

31. Gennari, O. *et al.* Investigation on cone jetting regimes of liquid droplets subjected to pyroelectric fields induced by laser blasts. *Appl Phys Lett* **106**, 054103 (2015).

32. Fujii, O., Honsali, K., Mizuno, Y. & Naito, K. Vibration of a water droplet on a polymeric insulating material subjected to AC voltage stress. *IEEE Transactions on Dielectrics and Electrical Insulation* **17**, 566–571 (2010).

33. Melcher, J. R. & Taylor, G. I. *ELECTROHYDRODYNAMICS: A REVIEW OF THE ROLE OF INTERFACIAL SHEAR STRESSES*. www.annualreviews.org.

34. Taylor, G., Disintegration of Water Drops in an Electric Field. Proceeding of the Royal Society, (1964) 383-397.

35. Mkhize, N. & Bhaskaran, H. Electrohydrodynamic Jet Printing: Introductory Concepts and Considerations. *Small Science* **2**, 2100073 (2022).

36. Mishra, S., Barton, K. L., Alleyne, A. G., Ferreira, P. M. & Rogers, J. A. High-speed and drop-on-demand printing with a pulsed electrohydrodynamic jet. *Journal of Micromechanics and Microengineering* **20**, (2010).

37. Barton, K., Mishra, S., Alleyne, A., Ferreira, P. & Rogers, J. Control of high-resolution electrohydrodynamic jet printing. *Control Eng Pract* **19**, 1266–1273 (2011).

38. Park, J. U. *et al.* High-resolution electrohydrodynamic jet printing. *Nat Mater* **6**, 782–789 (2007).

39. Onses, M. S., Sutanto, E., Ferreira, P. M., Alleyne, A. G. & Rogers, J. A. Mechanisms, Capabilities, and Applications of High-Resolution Electrohydrodynamic Jet Printing. *Small* vol. 11 4237–4266 Preprint at https://doi.org/10.1002/smll.201500593 (2015).

40. Ferraro, P., Coppola, S., Grilli, S., Paturzo, M. & Vespini, V. Dispensing nano-pico droplets and liquid patterning by pyroelectrodynamic shooting. *Nat Nanotechnol* **5**, 429–435 (2010).

41. Grilli, S. *et al.* Active accumulation of very diluted biomolecules by nano-dispensing for easy detection below the femtomolar range. *Nat Commun* **5**, (2014).

42. REGA, R. *et al.* Highly sensitive detection of low abundant molecules by pyro-electrohydro-dynamic jetting. in *Biophotonics in Point-of-Care* (eds. Canva, M. T., Giannetti, A., Moreau, J. & Altug, H.) 38 (SPIE, 2020). doi:10.1117/12.2564859.

43. Rega, R. *et al.* Detecting collagen molecules at picogram level through electric field-induced accumulation. *Sensors (Switzerland)* vol. 20 1–11 Preprint at https://doi.org/10.3390/s20123567 (2020).

44. Gennari, O. *et al.* A skin-over-liquid platform with compliant microbumps actuated by pyro-EHD pressure. *NPG Asia Mater* **11**, 1 (2019).

45. Rega, R. *et al.* Bipolar Patterning of Polymer Membranes by Pyroelectrification. *Advanced Materials* **28**, 454–459 (2016).

46. Mecozzi, L. *et al.* Simple and Rapid Bioink Jet Printing for Multiscale Cell Adhesion Islands. *Macromol Biosci* **17**, 1600307 (2017).

47. Gennari, O. *et al.* Pyroelectric Effect Enables Simple and Rapid Evaluation of Biofilm Formation. *ACS Appl Mater Interfaces* **10**, 15467–15476 (2018).

48. Rega, R., Muñoz Martinez, J. F. & Mugnano, M. *A pyroelectric-based system for sensing low abundant lactose molecules*.

49. Rega, R. *et al.* SensApp: a FET-open project for developing a supersensor able to detect Alzheimer's disease biomarkers in blood. in *Optical Methods for Inspection, Characterization, and Imaging of Biomaterials V* (eds. Ferraro, P., Ritsch-Marte, M., Grilli, S. & Hitzenberger, C. K.) 58 (SPIE, 2021). doi:10.1117/12.2596966.

50. Clark, M. F., Lister, R. M. & Bar-Joseph, M. ELISA techniques. in 742–766 (1986). doi:10.1016/0076-6879(86)18114-6.

51. Bugyi, Z. *et al.* Comparative study of commercially available gluten elisa kits using an incurred reference material. *Quality Assurance and Safety of Crops and Foods* **5**, 79–87 (2013).

52. Schena, M., Shalon, D., Davis, R. W. & Brown, P. O. Quantitative monitoring of gene expression patterns with a complementary DNA microarray. *Science (1979)* **270**, 467–470 (1995).

53. Safavieh, R., Pla Roca, M., Qasaimeh, M. A., Mirzaei, M. & Juncker, D. Straight SU-8 pins. *Journal of Micromechanics and Microengineering* **20**, (2010).

54. Romanov, V. *et al.* A critical comparison of protein microarray fabrication technologies. *Analyst* **139**, 1303–1326 (2014).

55. Helka, B. J. & Brennan, J. D. A guided materials screening approach for developing quantitative sol-gel derived protein microarrays. *J Vis Exp* 1–13 (2013) doi:10.3791/50689.

56. Theiler, P. M., Lütolf, F. & Ferrini, R. Non-contact printing of optical waveguides using capillary bridges. *Opt Express* **26**, 11934 (2018).

57. McWilliam, I., Kwan, M. C. & Hall, D. Inkjet printing for the production of protein microarrays. *Methods in Molecular Biology* **785**, 345–361 (2011).

58. Tkachenko, V. *et al.* High-Rate Accumulation of Tiny Aqueous Droplets Using a Pyroelectrohydrodynamic Jet System. *Adv Eng Mater* **24**, (2022).

59. Woodward, R. P. *Surface Tension Measurements Using the Drop Shape Method*.

60. Liu, H. & Cao, G. Effectiveness of the Young-Laplace equation at nanoscale. *Sci Rep* **6**, (2016).

61. Arthur W. Adamson, Alice P. Gast - Physical chemistry of surfaces-Wiley (1997).

62. Siqveland, L. M. & Skjæveland, S. M. Derivations of the young-laplace equation. *Capillarity* **4**, 23–30 (2021).

63. Vargaftik, N. B., Volkov, B. N. & Voljak, L. D. International Tables of the Surface Tension of Water. *J Phys Chem Ref Data* **12**, 817–820 (1983).

64. Camino, N. A., Pérez, O. E., Sanchez, C. C., Rodriguez Patino, J. M. & Pilosof, A. M. R. Hydroxypropylmethylcellulose surface activity at equilibrium and adsorption dynamics at the air-water and oil-water interfaces. *Food Hydrocoll* **23**, 2359–2368 (2009).

65. Baldino, N., Angelico, R., Caputo, P., Gabriele, D. & Rossi, C. O. Effect of high water salinity on the adhesion properties of model bitumen modified with a smart additive. *Constr Build Mater* **225**, 642–648 (2019).

66. Pérez, O. E., Sánchez, C. C., Pilosof, A. M. R. & Rodríguez Patino, J. M. Dynamics of adsorption of hydroxypropyl methylcellulose at the air-water interface. *Food Hydrocoll* **22**, 387–402 (2008).

67. Avranas, A. & Tasopoulos, V. Aqueous solutions of sodium deoxycholate and hydroxypropylmethylcellulose: Dynamic surface tension measurements. *J Colloid Interface Sci* **221**, 223–229 (2000).

68. Baldino, N., Mileti, O., Lupi, F. R. & Gabriele, D. Rheological surface properties of commercial citrus pectins at different pH and concentration. *LWT* **93**, 124–130 (2018).

69. Camino, N. A., Pérez, O. E., Sanchez, C. C., Rodriguez Patino, J. M. & Pilosof, A. M. R. Hydroxypropylmethylcellulose surface activity at equilibrium and adsorption dynamics at the air-water and oil-water interfaces. *Food Hydrocoll* **23**, 2359–2368 (2009).

70. Seta, L., Baldino, N., Gabriele, D., Lupi, F. R. & de Cindio, B. The effect of surfactant type on the rheology of ovalbumin layers at the air/water and oil/water interfaces. *Food Hydrocoll* **29**, 247–257 (2012).

71. Baeza, R., Pilosof, A. M. R., Sanchez, C. C. & Rodríguez Patino, J. M. Adsorption and rheological properties of biopolymers at the air-water interface. *AIChE Journal* **52**, 2627–2638 (2006).

72. Ward, A. F. H. & Tordai, L. Time-dependence of boundary tensions of solutions I. The role of diffusion in time-effects. *J Chem Phys* **14**, 453–461 (1946).

73. Graham, D. E. & Phillips, M. C. *Proteins at Liquid Interfaces Ill. Molecular Structures of Adsorbed Films*. (1979).

74. Camino, N. A., Pérez, O. E., Sanchez, C. C., Rodriguez Patino, J. M. & Pilosof, A. M. R. Hydroxypropylmethylcellulose surface activity at equilibrium and adsorption dynamics at the air-water and oil-water interfaces. *Food Hydrocoll* **23**, 2359–2368 (2009).

75. Gong, P. & Grainger, D. W. Comparison of DNA immobilization efficiency on new and regenerated commercial amine-reactive polymer microarray surfaces. *Surf Sci* **570**, 67–77 (2004).

76. George, R. A., Woolley, J. P. & Spellman, P. T. Ceramic capillaries for use in microarray fabrication. *Genome Res* **11**, 1780–1783 (2001).

77. Keleşoğlu, S., Meakin, P. & Sjöblom, J. Effect of Aqueous Phase pH on the Dynamic Interfacial Tension of Acidic Crude Oils and Myristic Acid in Dodecane. *J Dispers Sci Technol* **32**, 1682–1691 (2011).

78. Miller, R. *et al. Dynamics of protein and mixed proteinrsurfactant adsorption layers at the waterrfluid interface*. (2000).

79. Rodríguez Patino, J. M., Carrera Sánchez, C., Molina Ortiz, S. E., Rodríguez Niño, M. R. & Añón, M. C. Adsorption of Soy Globulin Films at the Air-Water Interface. *Ind Eng Chem Res* **43**, 1681–1689 (2004).

80. Roach, L. S., Song, H. & Ismagilov, R. F. *Controlling Nonspecific Protein Adsorption in a Plug-Based Microfluidic System by Controlling Interfacial Chemistry Using Fluorous-Phase Surfactants*. http://pubs.acs.org.

81. Razumovsky, L. & Damodaran, S. Surface. *Langmuir* **15**, 1392–1399 (1999).

82. Wagner1-, J. R. & Gueguen, J. *Effects of Dissociation, Deamidation, and Reducing Treatment on Structural and Surface Active Properties of Soy Glycinin*. *J. Agric. Food Chem* vol. 43 https://pubs.acs.org/sharingguidelines (1995).

83. Cornec, M., Cho, D. & Narsimhan, G. *Adsorption Dynamics of <alpha>-Lactalbumin and <beta>-Lactoglobulin at Air-Water Interfaces*. http://www.idealibrary.com (1999).

84. Benjamins, J., de Feijter, J. A., Evans, M. T. A., Graham, D. E. & Phillips, M. C. *Dynamic and Static Properties of Proteins Adsorbed at the Air/Water Interface*.

85. Razumovsky, L. & Damodaran, S. Surface. *Langmuir* **15**, 1392–1399 (1999).

Acknowledgments

Simona Itri acknowledges the EU funding within the Horizon 2020 Program, under the FET-OPEN Project “SensApp”, Grant Agreement n.829104.